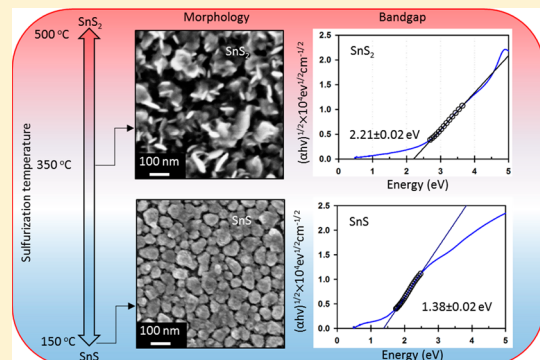


# Tuning the Phase and Optical Properties of Ultrathin $\text{SnS}_x$ Films

Y.-B. Yang,<sup>\*,†</sup> J. K. Dash,<sup>†</sup> Y. Xiang,<sup>†</sup> Y. Wang,<sup>‡</sup> J. Shi,<sup>‡</sup> P. H. Dinolfo,<sup>§</sup> T.-M. Lu,<sup>†</sup> and G.-C. Wang<sup>†</sup>

<sup>†</sup>Department of Physics, Applied Physics and Astronomy, and Center for Materials, Devices, and Integrated Systems, <sup>‡</sup>Department of Materials Science and Engineering, and Center for Materials, Devices, and Integrated Systems, and <sup>§</sup>Department of Chemistry and Chemical Biology, and Center for Materials, Devices, and Integrated Systems, Rensselaer Polytechnic Institute, 110 Eighth Street, Troy, New York 12180-3950, United States

**ABSTRACT:** Novel materials suitable for optoelectronics are of great interest due to limited and diminishing energy resources and the movement toward a green earth. We report a simple film growth method to tune the S composition,  $x$  from 1 to 2 in semiconductor ultrathin  $\text{SnS}_x$  films on quartz substrates, that is, single phase SnS, single phase  $\text{SnS}_2$ , and mixed phases of both SnS and  $\text{SnS}_2$  by varying the sulfurization temperature from 150 to 500 °C. Due to the ultrathin nature of the  $\text{SnS}_x$  films, their structural and optical properties are characterized and cross-checked by multiple surface-sensitive techniques. The grazing incidence X-ray diffraction (GIXRD) shows that the single phase SnS forms at 150 °C, single phase  $\text{SnS}_2$  forms at 350 °C and higher, and mixed phases of SnS and  $\text{SnS}_2$  form at temperature between. GIXRD shows structures of SnS film and  $\text{SnS}_2$  film are orthorhombic and 2H hexagonal, respectively. To complement the GIXRD, the reflection high energy electron diffraction pattern analysis shows that both pure phases are polycrystalline on the surface. Raman spectra support existence of pure phase SnS, pure phase  $\text{SnS}_2$ , and mixed phases of SnS and  $\text{SnS}_2$ . X-ray photoelectron spectroscopy reveals that the near surface stoichiometry of both single phase SnS and single phase  $\text{SnS}_2$  are close to Sn/S ratios of 1:1 and 1:2, respectively. UV-vis spectroscopy shows the optical absorption coefficient of SnS film is higher than  $10^5 \text{ cm}^{-1}$  above the optical bandgap of  $1.38 \pm 0.02 \text{ eV}$ , an ideal optical absorber. A two-terminal device made of SnS film grown on  $\text{SiO}_2$  substrates shows good photoresponse. The  $\text{SnS}_2$  has an optical bandgap of  $2.21 \pm 0.02 \text{ eV}$ . A photoluminescence (PL) peak of  $\text{SnS}_2$  film is observed at  $\sim 542 \text{ nm}$ . Time-resolved PL of the single phase ultrathin  $\text{SnS}_2$  film indicates a carrier lifetime of 1.62 ns, longer than sub nanosecond lifetime from multilayer  $\text{SnS}_2$ . Our comprehensive results show that ultrathin SnS and  $\text{SnS}_2$  films have the required properties for potential photodetectors and solar cell applications but consume much less material as compared with current thin film devices.



## I. INTRODUCTION

Layered metal dichalcogenide films with intrinsic optical band gaps in the range of 1 to 3 eV have attracted considerable interest for potential applications in optoelectronics and photovoltaics. Semiconductor  $\text{SnS}_x$  is one of these promising materials that possess the advantages of being nontoxic to the environment and earth-abundant. Tin sulfides can be formed in several phases including SnS,  $\text{SnS}_2$ , and  $\text{Sn}_2\text{S}_3$  due to their different heats of formation and therefore depend on the relative amounts of sulfur, tin, and temperature during film growth. Depending on the Sn concentration, the  $\text{SnS}_x$  film can be either an n- or p-type semiconductor. Among the  $\text{SnS}_x$ , a thin SnS film has many desired properties for photovoltaic applications such as an optical band gap of  $\sim 1.0$  to  $\sim 1.5$  eV, a high absorption coefficient, and an intrinsic p-type semiconductor nature. SnS can therefore be used as an absorber layer in solar-based devices. For thin  $\text{SnS}_2$  films, the optical band gap is higher around 2.2 eV and is an n-type semiconductor and can be considered as a window layer in solar cells.

In the past decade, various physical and chemical routes were developed and aimed to grow  $\text{SnS}_x$  thin films that are single-

phase and exhibit large grains. Vast amount of SnS thin film work has been reviewed.<sup>1</sup> Methods for the deposition of SnS thin film on amorphous substrates such as glass, include sulfurization of predeposited Sn by thermal evaporation,<sup>2</sup> DC sputtering,<sup>3,4</sup> electrodeposition,<sup>5</sup> thermal evaporation<sup>6–8</sup> or e-beam evaporation<sup>9</sup> of SnS powders, pulse laser deposition of SnS<sub>x</sub> target and post annealing,<sup>10</sup> molecular beam epitaxy,<sup>11</sup> multilayered solid state reaction,<sup>12</sup> atomic layer deposition (ALD),<sup>13,14</sup> ionic adsorption and reaction,<sup>15</sup> and vapor transport deposition.<sup>16</sup> Growth methods determine whether the polycrystalline SnS thin films are dominant (111) or (040) orientation, and as a result the values of optical band gap vary over a wide range.

For  $\text{SnS}_2$ , researchers report exfoliated bulk  $\text{SnS}_2$ ,<sup>17</sup> chemical vapor deposition of nanocrystals,<sup>18–21</sup> chemical vapor transport,<sup>22</sup> coevaporation of Sn and S nanoflakes,<sup>23</sup> and hydrothermal growth of nanoflowers.<sup>24,25</sup> Methods used to grow continuous  $\text{SnS}_2$  thin films on amorphous substrates such as

Received: April 6, 2016

Revised: May 25, 2016



$\text{SiO}_2/\text{Si}$  are less reported. Few examples include molecular beam epitaxy,<sup>26</sup> plasma enhanced chemical vapor deposition,<sup>27</sup> and ALD.<sup>13</sup>

As for the demonstration of applications, the efficiencies of SnS-based thin film solar cells have been reported from less than 1% to 4.36%.<sup>28</sup> Other optoelectronic properties of SnS, such as photoresponse to light<sup>4,29</sup> and gas,<sup>30</sup> have been demonstrated. Thin  $\text{SnS}_2$  film has a higher optical band gap ranging from  $\sim 1.8$  to  $\sim 3.8$  eV and is attractive as a window layer in solar cells.  $\text{SnS}_2$  has been demonstrated to have high carrier mobility,<sup>17</sup> high on-off current ratios in field effect transistors,<sup>17,31,32</sup> and fast photocurrent response times of a few microsecond<sup>18</sup> and millisecond.<sup>21,33</sup> In order to improve the efficiency and photoresponse, the limiting factors in the materials' properties need to be identified and overcome. Examples are the short minority lifetime and the short diffusion length, which are directly related to the crystalline quality of the SnS such as grain size, density of grain boundaries, and the surface/interface roughness. Another example is the conduction type in SnS or  $\text{SnS}_2$  is effected by the stoichiometry inhomogeneity and sulfur content.

We report a simple way to prepare single phase SnS films, single phase  $\text{SnS}_2$  films, and films containing mixed phases of SnS and  $\text{SnS}_2$  films by simply changing the sulfurization temperature of ultrathin Sn films predeposited on amorphous quartz substrates. Our method is controllable, simple, and inexpensive because the thickness of the SnS and  $\text{SnS}_2$  films depends on the starting thickness of Sn film that are  $\sim 20$  nm in this report. For a low substrate temperature of  $150\text{ }^\circ\text{C}$ , a single phase SnS is formed, for temperatures of  $200$  or  $225\text{ }^\circ\text{C}$ , a mixed phase SnS and  $\text{SnS}_2$  is formed, and for higher temperatures of  $350$  or  $500\text{ }^\circ\text{C}$ , a single phase  $\text{SnS}_2$  is formed. Both temperatures for forming single phase SnS and single phase  $\text{SnS}_2$  are lower than past reports. All sulfurized  $\text{SnS}_x$  films ( $\sim 50$  nm) are about two to three times thicker than the starting Sn film thickness. Multiple techniques were used to evaluate the ultrathin films' optoelectronic properties. The crystal structures, chemical compositions, and vibrational modes of these  $\text{SnS}_x$  films were measured by grazing incidence X-ray diffraction (GIXRD), reflection high energy electron diffraction (RHEED), atomic force microscopy (AFM), scanning electron microscopy (SEM), X-ray photoelectron spectroscopy (XPS), and Raman spectroscopy. The optical property was characterized by ultraviolet-visible-near-infrared spectroscopy (UV-vis-NIR), photoluminescence (PL), and time-resolved PL. A simple two-terminal device was used to measure the photoresponse of the SnS films. Our results show that many physical properties and performances of ultrathin SnS and  $\text{SnS}_2$  films are similar to or better than thicker films and require much less material consumption. The ability to tune the  $\text{SnS}_x$  phases may be useful for thin film solar cells using SnS as an absorber and  $\text{SnS}_2$  as a window layer. In addition, applications of  $\text{SnS}_2$  can be broadened to fast photodetectors or high performance batteries by producing hybrid  $\text{SnS}_2$  nanostructures with other materials.

## II. EXPERIMENTAL SECTION

Ultrathin Sn ( $\sim 20$  nm thick) films on amorphous quartz substrates were prepared by evaporating Sn pellets (99.99% purity) with a deposition rate of  $1\text{ \AA/s}$  in a high vacuum chamber with a base pressure in the midrange of  $10^{-8}$  Torr. The single phase SnS, mixed phase SnS and  $\text{SnS}_2$  (either SnS dominant or  $\text{SnS}_2$  dominant), and single phase  $\text{SnS}_2$  films were prepared by sulfurizing the Sn film at a fixed temperature

ranging from  $150$  to  $500\text{ }^\circ\text{C}$  in a furnace. The schematic in Figure 1a shows the arrangement in the furnace. The ultrathin

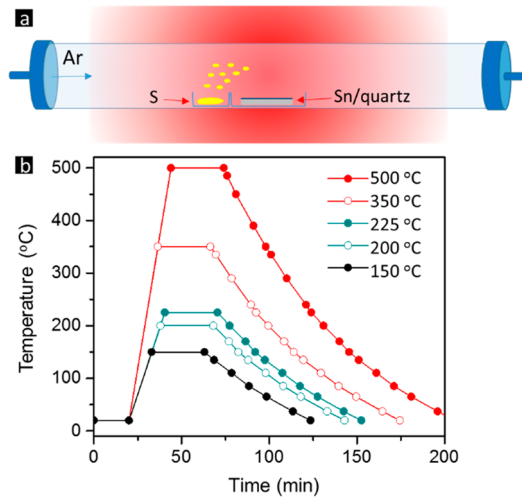


**Figure 1.** Schematic (not to scale) of the experimental setup for the synthesis of  $\text{SnS}_x$  films in a one zone furnace. (a) Sulfurization of ultrathin Sn film predeposited on quartz substrate using sulfur vapor in a furnace under Ar flow, and (b) temperature of S and Sn/quartz substrate vs time during synthesis of  $\text{SnS}_x$  films.

Sn film on a quartz substrate was placed in a quartz boat ( $100 \times 45 \times 20$  mm) and was positioned near the center of the furnace where the temperature is most stable and closest to the preset temperature measured by a pair of thermocouple wires. The sulfur powder (99.98% purity, 2.3000 g) placed in a quartz boat was positioned near the edge of the quartz tube where the temperature is lower than the preset temperature. Both were positioned at room temperature prior to turning on the furnace. The quartz tube was purged with an ultrahigh purity (99.999%) grade Ar gas with a flow rate of 950 sccm from the side of the sulfur quartz boat to the quartz boat containing ultrathin Sn film/quartz substrate. After 20 min of Ar gas purging at 950 sccm, the Ar gas flow rate was reduced to 200 sccm, while the furnace was gradually heated up with a ramping rate of  $10\text{ }^\circ\text{C/min}$  from room temperature to one of the preset temperatures:  $150$ ,  $200$ , or  $225\text{ }^\circ\text{C}$ . The ramping rate was doubled to  $20\text{ }^\circ\text{C/min}$  for the preset temperatures  $350$  or  $500\text{ }^\circ\text{C}$ . The temperature ramping was managed using a programmable temperature controller (Eurotherm 2116 PID) attached to the furnace. The temperature was measured using a type K thermocouple placed near the center of the furnace between the quartz tube and the ceramic liner of the furnace. After 30 min of synthesis at the preset temperature, the furnace filament current was gradually reduced to zero over 5–6 min and the quartz tube cooled down to room temperature. The temperature variation throughout this process is shown in Figure 1b. Ar gas purging was continuous during the entire heating and cooling processes.

To characterize the crystal structure and average vertical crystalline size of the synthesized ultrathin  $\text{SnS}_x$  films, GIXRD instead of conventional X-ray diffraction scans were collected using a PanAlytical X'Pert Pro diffractometer. The X-ray wavelength was  $0.15405\text{ nm}$ . A point detector with a  $0.013^\circ$  scanning step size and a  $0.25\text{ s}$  counting time at each step, was used to collect X-ray diffraction intensity. The incident angle was fixed at  $1.5^\circ$  while  $2\theta$  was varied. The detector scanned over  $2\theta$  in the scattering plane that contained the incident X-ray

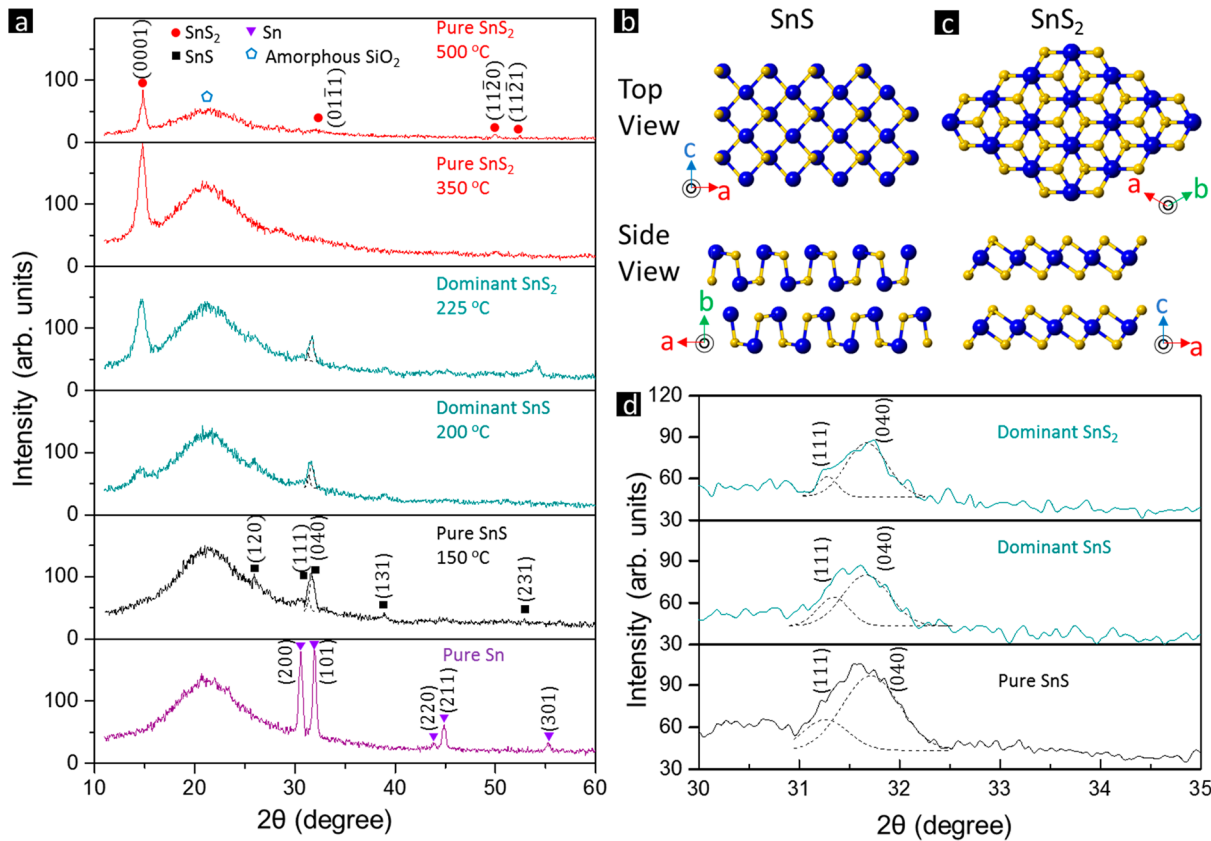


**Figure 2.** (a) Grazing incidence X-ray diffraction scans from ~20 nm thick Sn film deposited on quartz substrate and SnS<sub>x</sub> films synthesized from ~20 nm thick Sn on quartz substrate at 150, 200, 225, 350, and 500 °C for 30 min, (b) top and side views of a ball model of SnS, (c) top and side views of a ball model of SnS<sub>2</sub>, and (d) expanded view of GIXRD intensity vs theta from 30° to 35° showing the fit of (111) and (040) peaks.

and the surface normal while the source and sample stage were fixed.

To examine the near surface structure of ultrathin single phase SnS and SnS<sub>2</sub> films RHEED was used. The RHEED patterns were produced by 15 keV electrons (RDA-003G electron gun) diffracted from the top few nm of the sample and then projected onto a 6 in. phosphor screen. The patterns were recorded by a charged coupled device camera placed outside the vacuum chamber. The sample holder can be rotated in-plane allowing for RHEED patterns to be collected at different azimuthal angles.

The surface morphologies of synthesized ultrathin single phase SnS and SnS<sub>2</sub> films were imaged by field emission SEM (Zeiss Supra 55 FE) and AFM (PSI XE100) in contact mode. The cantilever (Olympus-AC240TS) used in AFM experiments has a tip radius of ~7 nm, a force constant of 2 N/m and a resonant frequency of 70 kHz.

The near surface compositions of the ultrathin single phase SnS and SnS<sub>2</sub> films were measured by XPS. The nearly monochromatic X-ray Mg K source (PHI model 04-151) had a primary energy of 1253.6 eV. The operation conditions of the X-ray source were 270 W with a 10 kV high-voltage bias and a 27 mA emission current. A double pass cylindrical mirror energy analyzer (PHI model 15-255G) was used to detect the photoelectrons emitted from the sample surface. Each spectrum was an average of 40 repeated scans at a passing energy of 50 eV.

Vibrational modes were identified from Raman spectra collected from ultrathin SnS<sub>x</sub> films using a confocal Raman microscope (Witec Alpha 300). The laser wavelength and

power used were 532.1 nm and 17 mW, respectively. A 100× objective lens produced a spot size of ~721 nm (=1.22 × wavelength/numerical aperture of 0.9 for the 100× objective lens). The spectral resolution and step size used in Raman scattering data collection were 0.02 and 0.7 cm<sup>-1</sup>, respectively.

UV-vis-NIR transmission and reflectance spectra were collected to determine the optical band gap of the ultrathin SnS<sub>x</sub> films on quartz substrates. The spectra were obtained using a UV/vis spectrometer (PerkinElmer Lambda 950). The transmission spectra were obtained in air with slides held normal to the incident light beam and corrected for the quartz background. Specular reflectance spectra were obtained at a near-normal incidence angle of 6°.

The PL and time-resolved PL signals were collected from single phase SnS<sub>2</sub> film using a customized time-resolved PL system. A pulsed diode laser (Picoquant) with 405 nm wavelength was used as the excitation source. The pulse width and pulse frequency were 50 ps and 20 MHz, respectively. The estimated power density in the area with 1 μm laser spot diameter was ~0.3 MW/cm<sup>2</sup>. The incident laser was directed onto the sample through an inverted microscope (Nikon Eclipse Ti). The PL signal was then directed into a monochromator (Princeton Instruments SP-2358), inside which the grating wavelength was fixed at the PL peak position. The scanning resolution of the monochromator was 0.001 nm and the slit width was fixed to <2 mm. A single photon Si detector (Picoquant PDM) was aligned at the exit port of the monochromator to count photons and to collect steady state PL and time-resolved PL data with a 0.025 ns time resolution.

The current–voltage ( $I$ – $V$ ) measurement of ultrathin single phase SnS films was carried out using a Keithley 2400 source meter and two-probe Indium contacts with a separation distance of 7.6 mm. The photocurrent response was measured using a lamp with a broad range of wavelengths ranging from 500 to 1000 nm with a peak around 750 nm and a full-width-at-half-maximum (fwhm) of  $\sim 300$  nm. The total power output from the lamp can be varied from 0 to  $0.9 \mu\text{W}/\text{cm}^2$ .

### III. RESULTS AND DISCUSSION

**III.A. Structure of Sn and  $\text{SnS}_x$  Films Characterized by Grazing Incidence X-ray Diffraction.** All data presented were collected by GIXRD because the intensity collected from conventional X-ray diffraction of our ultrathin films was too low for analysis. Figure 2a shows the GIXRD spectra collected from the 20 nm thick Sn films deposited on quartz substrates at room temperature as well as  $\text{SnS}_x$  films/quartz substrates sulfurized and grown at 150, 200, 225, 350, and 500 °C for 30 min. The GIXRD scan of pure Sn shown in the bottom of Figure 2a has peaks at  $30.60 \pm 0.01^\circ$  and  $31.98 \pm 0.01^\circ$ . These peak positions are consistent with Sn(200) and Sn(101) for tetragonal Sn (beta Sn,  $\alpha = \beta = \gamma = 90^\circ$ ) with lattice constants  $a = 5.838 \text{ \AA}$ ,  $b = 5.838 \text{ \AA}$ , and  $c = 3.185 \text{ \AA}$ . The second curve from the bottom in Figure 2a reveals that the film synthesized at 150 °C has peaks at  $25.94 \pm 0.01^\circ$ ,  $31.29 \pm 0.02^\circ$ ,  $31.73 \pm 0.01^\circ$ ,  $38.89 \pm 0.03^\circ$ , and  $54.03 \pm 0.03^\circ$ . These peaks labeled (120), (111), (040), (131), and (231) are consistent with a single phase orthorhombic structure of SnS (space group Pbnm) with lattice constants  $a = 4.33 \text{ \AA}$ ,  $b = 11.190 \text{ \AA}$ , and  $c = 3.98 \text{ \AA}$ . Figure 2b shows the top and side views of a ball model of the SnS structure. The side view shows that SnS is a layered compound consisting of double layers of Sn and S with its  $b$ -axis perpendicular to the substrate. Figure 2d provides a closer look at the broad peak from  $31^\circ$  to  $32^\circ$  for pure SnS, dominant SnS, and dominant  $\text{SnS}_2$  films. Gaussian deconvolution shows two peaks, (111) and (040) whose  $2\theta$  angles are  $31.3^\circ$  and  $31.7^\circ$ , respectively. The films synthesized at 350 and 500 °C each have a peak at  $14.91 \pm 0.01^\circ$ . This peak labeled (0001) in Figure 2a is consistent with a single phase  $\text{SnS}_2$  (space group  $P\bar{3}m1$ ) of hexagonal (2H) structure with lattice constants  $a = b = 3.645 \text{ \AA}$  and  $c = 5.891 \text{ \AA}$ . A ball model of  $\text{SnS}_2$  is shown in Figure 2c. Note the  $c$ -axis of the  $\text{SnS}_2$  film is perpendicular to the substrate. The film synthesized at 200 °C has a mixture of dominant SnS phase and a minor  $\text{SnS}_2$  phase, whereas the film synthesized at 225 °C has a minor SnS phase and a dominant  $\text{SnS}_2$  phase. Judging from Figure 2a, the phase of  $\text{SnS}_x$  changes depending on the sulfurization temperature. Table 1 lists the growth temperature and  $2\theta$  angles for Bragg peaks ( $hkl$ ).

The Bragg peak position obtained from a  $\theta/2\theta$  scan provides information about the out-of-plane orientation of a film. The fwhm of a Bragg peak intensity profile after deconvolution with the appropriate instrument response function is approximately inversely proportional to the average size of the ordered regions/crystallite in the direction perpendicular to the substrate. The fwhm does not provide crystallite size in the horizontal or parallel to the film surface. The average crystallite sizes of films in the nearly vertical direction calculated from the fwhm using the Scherrer formula are listed in Table 1. The sizes were obtained from the pure Sn(200) peak, SnS(040) peak, and  $\text{SnS}_2$ (0001) peak of the films synthesized at various temperatures. The crystallite size in the SnS film synthesized at 150 °C is  $\sim 13$  nm. As the synthesis temperature increases the crystallite size in the SnS film increases and reaches  $\sim 15$  nm at

**Table 1. List of Phases, Growth Temperature, GIXRD Peaks ( $hkl$ ),  $2\theta$  Angle, the Full-Width-at-Half Maximum (fwhm) of GIXRD Peaks ( $hkl$ ), and Near Vertical Average Crystallite Sizes of Sn and  $\text{SnS}_x$  Films on Quartz Substrates Calculated from Scherrer Formula**

sample	growth temp (°C)	( $hkl$ ) and $2\theta$ (deg)	fwhm (deg)	avg vertical crystallite size (nm)
Sn	20	(200); $30.60 \pm 0.01$	$0.46 \pm 0.05$	$17.76 \pm 1.75$
SnS	150	(111); $31.29 \pm 0.02$ (040); $31.73 \pm 0.01$	$0.52 \pm 0.08$ $0.63 \pm 0.03$	$15.86 \pm 2.11$ $13.11 \pm 1.31$
dominant SnS and minor $\text{SnS}_2$	200	(111); $31.34 \pm 0.03$ (040); $31.66 \pm 0.01$ (0001); $14.67 \pm 0.05$	$0.46 \pm 0.10$ $0.54 \pm 0.03$ $2.06 \pm 0.98$	$17.93 \pm 3.21$ $15.29 \pm 1.97$ $3.88 \pm 1.26$
minor SnS and dominant $\text{SnS}_2$	225	(111); $31.28 \pm 0.03$ (040); $31.67 \pm 0.01$ (0001); $14.71 \pm 0.01$	$0.38 \pm 0.10$ $0.54 \pm 0.07$ $0.93 \pm 0.02$	$21.71 \pm 4.52$ $15.29 \pm 1.75$ $8.61 \pm 0.24$
$\text{SnS}_2$	350	(0001); $14.73 \pm 0.01$	$0.83 \pm 0.01$	$9.57 \pm 0.17$
$\text{SnS}_2$	500	(0001); $14.83 \pm 0.01$	$0.57 \pm 0.03$	$13.93 \pm 0.87$

225 °C. This size is approximately the thickness of the original Sn film. At 200 °C the  $\text{SnS}_2$  crystallites emerge with a size of  $\sim 4$  nm. As the temperature increases further the  $\text{SnS}_2$  crystallite size gradually increases to  $\sim 10$  nm at 350 °C and  $\sim 14$  nm at 500 °C, while the SnS associated peaks (111) and (040) disappear at 350 °C. The near vertical average crystallite size is limited by the initial Sn film thickness of  $\sim 20 \pm 2$  nm measured by line scans of AFM to be presented in Figure 4a later. Note the average vertical crystallite size is not the film thickness. The thickness of sulfurized  $\text{SnS}_x$  film is about two times thicker than the starting thickness of pure Sn as seen from SEM side view images shown in Figure 4g,h.

**$\text{SnS}(040)$  Film.** GIXRD scan reveals a single phase SnS with a strong (040) peak at a lower sulfurization temperature of 150 °C, and a single phase  $\text{SnS}_2$  film with a strong (0001) peak at sulfurization temperatures of 350 °C and above. At 150, 200, and 225 °C, additional (120), (131), and (231) peaks were observed in the mixed phase films. In Table 2 we compared our results with other works, that is, predeposition of Sn on a substrate and then sulfurization. The methods used for predeposited Sn in other works, include thermal evaporation,<sup>2</sup> sputtering,<sup>4,29</sup> and electrodeposition<sup>5</sup> of Sn, and sulfurized Sn at temperatures higher than 150 °C. These SnS films were much thicker than our 50 nm SnS film. Due to the fact these films were thicker, other orientations like (111) and (101) in addition to (040) were developed and observed.

We also compare our observed (040) orientation of the SnS film grown by sulfurization of predeposited ultrathin Sn with literature reports that used different methods. The (040) orientation was also observed in SnS films grown on glass substrates by thermal evaporation of SnS powders,<sup>6,34</sup> and pulsed laser deposition of SnS film on amorphous  $\text{SiO}_2$  substrate with a sulfur-rich Sn–S target.<sup>35</sup> Other methods such as thermal evaporation of SnS powders,<sup>6,7,36</sup> RF sputtering from an SnS target,<sup>37,38</sup> and atomic layer deposition<sup>13,14</sup> also

**Table 2. Comparison of Orientations of SnS and  $\text{SnS}_2$  Films Observed in Present Work Using Sulfurization of Pre-Thermally-Deposited Sn Films, with Other Works Including Sulfurization of Pre-Deposited Sn Films by Either Thermal, Sputtering, or Electrodeposition, and Atomic Layer Deposition (ALD) of SnS and  $\text{SnS}_2$**

method	thickness (nm)	temp (°C)	SnS film		$\text{SnS}_2$ film	
			orientation	temp (°C)	orientation	
this work	~50	150	(040), (111), (120)	350, 500	(0001)	
sulfurization of predeposited Sn <sup>2</sup>	900	200–400	(111), (021), (171)	200–400	weak $\text{SnS}_2$	
sulfurization of sputtered deposited Sn <sup>4</sup>	400	200	(110), (120), (021), (101), (111), (040), (131)			
sulfurization of electrodeposited Sn <sup>5</sup>	<1200	330	(111), (101), (040)			
ALD <sup>14</sup>	97–330	120–200	(111), (101), (040)			
ALD <sup>13</sup>	~50	160, 180	(111), (120)	140, 150	(0001)	

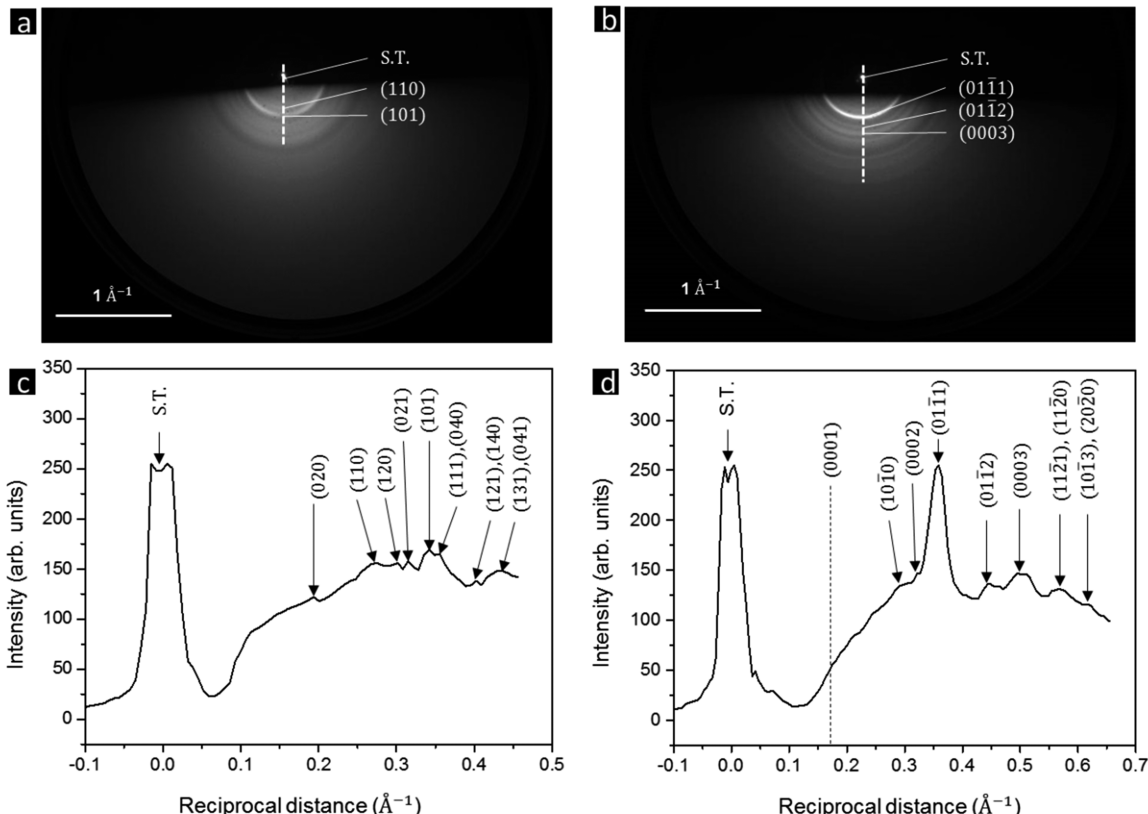


**Figure 3.** Reflection high energy electron diffraction patterns for (a) SnS film synthesized at 150 °C and (b)  $\text{SnS}_2$  films synthesized at 350 °C. Intensity scan along the radial direction of (c) SnS film synthesized at 150 °C and (d)  $\text{SnS}_2$  film synthesized at 350 °C. S.T. stands for the straight-through beam.

show (111) and (101) orientations in addition to the (040) orientation.

As shown in Table 2, the (040) and (111) orientations experimentally observed in SnS films appear to be the majority. The density functional theory (DFT) calculations have shown that for SnS the surface energy depends on orientation.<sup>39</sup> The (100) orientation has the lowest surface energy of 9.6 meV/Å<sup>2</sup>, jumping to about 25 meV/Å<sup>2</sup> for the (201) and (111) orientations. Note the (100), (201), and (111) orientations obtained from DFT are equivalent to (040), (120), and (111) observed in our XRD patterns. In DFT calculations,  $a = 10.97 \text{ \AA}$ ,  $b = 3.95 \text{ \AA}$ , and  $c = 4.18 \text{ \AA}$ . In terms of the dominant facet in an equilibrium crystal using the Wulff construction,<sup>40</sup> the (100), (111), and (201) have 52, 26, and 4.5% of the total surface area. The dominant (100) orientation is parallel to the SnS layer; therefore, we conclude that there is no Sn–S bond breaking and the interaction between SnS layers is weakly mediated by

the “lone pair” electrons.<sup>39</sup> Our GIXRD data (nearly out-of-plane Bragg intensity) shows a strong (040) orientation in the SnS film (which is parallel to the (100) orientation). The next lowest energy (111) and (102) orientations are also observed in our GIXRD measurement. From our RHEED ring patterns to be presented in the next section, these orientations on the surface are distributed randomly in all directions.

**$\text{SnS}_2(0001)$  Films.**  $\text{SnS}_2$  has a higher heat of formation ( $-40.0 \pm 4.0 \text{ kcal/mol}$ ;  $-1.73 \text{ eV}$ ) as compared with SnS ( $-25.1 \pm 1.2 \text{ kcal/mol}$ ;  $-1.09 \text{ eV}$ ),<sup>41</sup> and it is more stable once formed. However, higher temperatures are required to form  $\text{SnS}_2$ . In our ultrathin film, the temperature required to form single phase  $\text{SnS}_2$  is higher ( $\sim 350 \text{ }^\circ\text{C}$ ) than needed to form single phase SnS ( $\sim 150 \text{ }^\circ\text{C}$ ). For temperatures less than 350 °C, SnS and  $\text{SnS}_2$  phases coexist. The trend in our temperature-dependent phase change differs from that obtained from ALD where the growth temperature of SnS(111) is at 160 °C and is

higher than 140 °C of SnS<sub>2</sub>(001)<sup>13</sup> (see Table 2). The difference may be due to the sensitive chemical reactions between Sn-containing precursors and hydrogen sulfide used in ALD. In pyrolysis, instead of changing the temperature, the change of phase from SnS to SnS<sub>2</sub> can be achieved by changing the reaction conditions. An example is the formation of SnS(040) nanosheets, which are made by a single source precursor and can be changed into spherical SnS<sub>2</sub>(001) nanoplates by changing the chemicals used during the reaction at ~280 °C.<sup>42</sup>

Inferred from the results listed in Tables 1 and 2, our sulfurization of ultrathin Sn films has several advantages: (1) The pure SnS film can be achieved at 150 °C, the lowest temperature among predeposition of Sn and then sulfurization; (2) The pure SnS<sub>2</sub> film can be obtained at 350 °C. Other works either have mixed-phase SnS and SnS<sub>2</sub> over a wide range of temperatures (200–400 °C)<sup>2</sup> or did not report the SnS<sub>2</sub> phase;<sup>43</sup> and (3) In order to tune the phases the film involved needs to be thin because the sulfurization of Sn starts from the surface of Sn. For thicker Sn films, either the sulfurization temperature has to be higher, the sulfurization time needs to be longer, or both.

**III.B. Near Surface Structure of SnS and SnS<sub>2</sub> Films Characterized by Reflection High Energy Electron Diffraction.** Due to the fact that sulfurization most likely started from the surface of Sn, we examined the near surface structure and texture of ultrathin SnS and SnS<sub>2</sub> films using transmission-mode RHEED.<sup>43</sup> For a 15 keV electron energy used in our experiment the electron penetration length is a few nm. For both the SnS film grown at 150 °C and the SnS<sub>2</sub> film grown at 350 °C, we observed concentric diffraction rings centered on the straight-through (S.T.) spot, as shown in Figure 3a and b, respectively, at one azimuthal angle. The existence of rings in the RHEED pattern implies that both our samples are polycrystalline as expected when grown on amorphous substrates.<sup>43</sup> These patterns differ from the stripe patterns observed for single crystal SnS<sub>2</sub><sup>44,45</sup> and 30 monolayer thick SnS<sub>2</sub> films grown on single crystal mica.<sup>26</sup> The fact that the rings are uniform in intensity indicates that the grain orientations are completely random in all directions.<sup>46,47</sup> RHEED patterns were taken at various in-plane azimuthal angles and showed similar rings. The radius  $r$  of the rings on the screen is determined by the angle between the outgoing electron beam and the incident electron beam or the  $2\theta$  angle through the relation

$$r = L \cdot \tan(2\theta)$$

where  $L$  is the distance from the location where the incident electron beam strikes on the sample surface to the phosphor screen. The  $2\theta$  angle is related to the interplanar distance  $d_{hkl}$  through the Bragg condition

$$2d_{hkl} \cdot \sin \theta = \lambda$$

where  $\lambda$  is the wavelength of the incident electrons. In our experiment, we used 15 keV electrons as the source. The calculated corresponding wavelength is 0.1 Å through the de Broglie relation

$$\lambda = \frac{h}{p} = \frac{h}{\sqrt{2mE}} = \sqrt{\frac{150.4}{E(\text{eV})}}$$

where  $h$  is Planck's constant and  $p$  is electron's momentum. Because the incident angle is very small in our experiment, we can use the small angle approximation

$$\tan(2\theta) \approx 2 \sin \theta \approx 2\theta$$

Therefore, the radius  $r$  on the screen is approximately inversely proportional to the interplanar distance  $d_{hkl}$  and proportional to the magnitude of lattice vector  $\vec{K}$  in the reciprocal space,

$$r \approx \frac{L\lambda}{d_{hkl}} \propto K$$

In the RHEED pattern analysis, we measured the radius  $r$  of each ring on the RHEED images in units of pixels using ImageJ software. The relationship between one pixel and the corresponding reciprocal distance in units of Å<sup>-1</sup> has already been calibrated using the RHEED pattern of an epitaxial CdTe(100) film on a single crystal GaAs(100) substrate with a known lattice constant under the same experimental conditions.<sup>48</sup> In this way we obtained the scale bar for both the SnS and SnS<sub>2</sub> RHEED patterns in Figure 3a,b. The intensity along the radial direction shown as a white dashed line in Figure 3a is plotted as a function of reciprocal distance shown in Figure 3c for the SnS film. A similar radial intensity plot is shown in Figure 3d for the SnS<sub>2</sub> film.

Each peak in Figure 3c,d corresponds to a diffraction ring in the RHEED patterns. The positions of those peaks were found by first subtracting the background intensity and then fitting each peak using a Gaussian function. The background for a given point on a ring is taken to be the diffraction intensity slightly outside of the ring on the line from the point to the center of the rings.<sup>49</sup> Finally, we took the center of the Gaussian function as the position of each peak. A reciprocal distance is related to the lattice constants of a crystal through the relation:

$$\begin{aligned} K^2 &= \frac{1}{d^2} \\ &= \frac{h^2}{a^2} + \frac{k^2}{b^2} + \frac{l^2}{c^2} \quad (\text{for orthorhombic crystal system}) \end{aligned}$$

and

$$\begin{aligned} K^2 &= \frac{1}{d^2} \\ &= \frac{4}{3} \left( \frac{h^2 + hk + k^2}{a^2} \right) + \frac{l^2}{c^2} \\ &\quad (\text{for hexagonal crystal system}) \end{aligned}$$

As mentioned in the previous section, SnS has an orthorhombic structure with lattice constants:  $a = 4.33$  Å,  $b = 11.19$  Å,  $c = 3.98$  Å. SnS<sub>2</sub> has a hexagonal structure with lattice constants:  $a = 3.645$  Å,  $b = 3.645$  Å,  $c = 5.891$  Å. Using these values, we calculated the expected radii of rings associated with different  $(hkl)$  indices in reciprocal space for both SnS and SnS<sub>2</sub>. By matching them with the measured positions of peaks, we found the index for each peak, as shown in Figure 3c,d. Most peaks can be easily identified while some peaks far away from the straight-through peak are not resolved due to low signal-to-noise ratios. All peaks with low  $(hkl)$  indices observed in GIXRD were observed by RHEED. Due to the strong electron scattering, more  $(hkl)$  peaks are observed by RHEED than GIXRD from SnS, for example, (020), (101), (021),

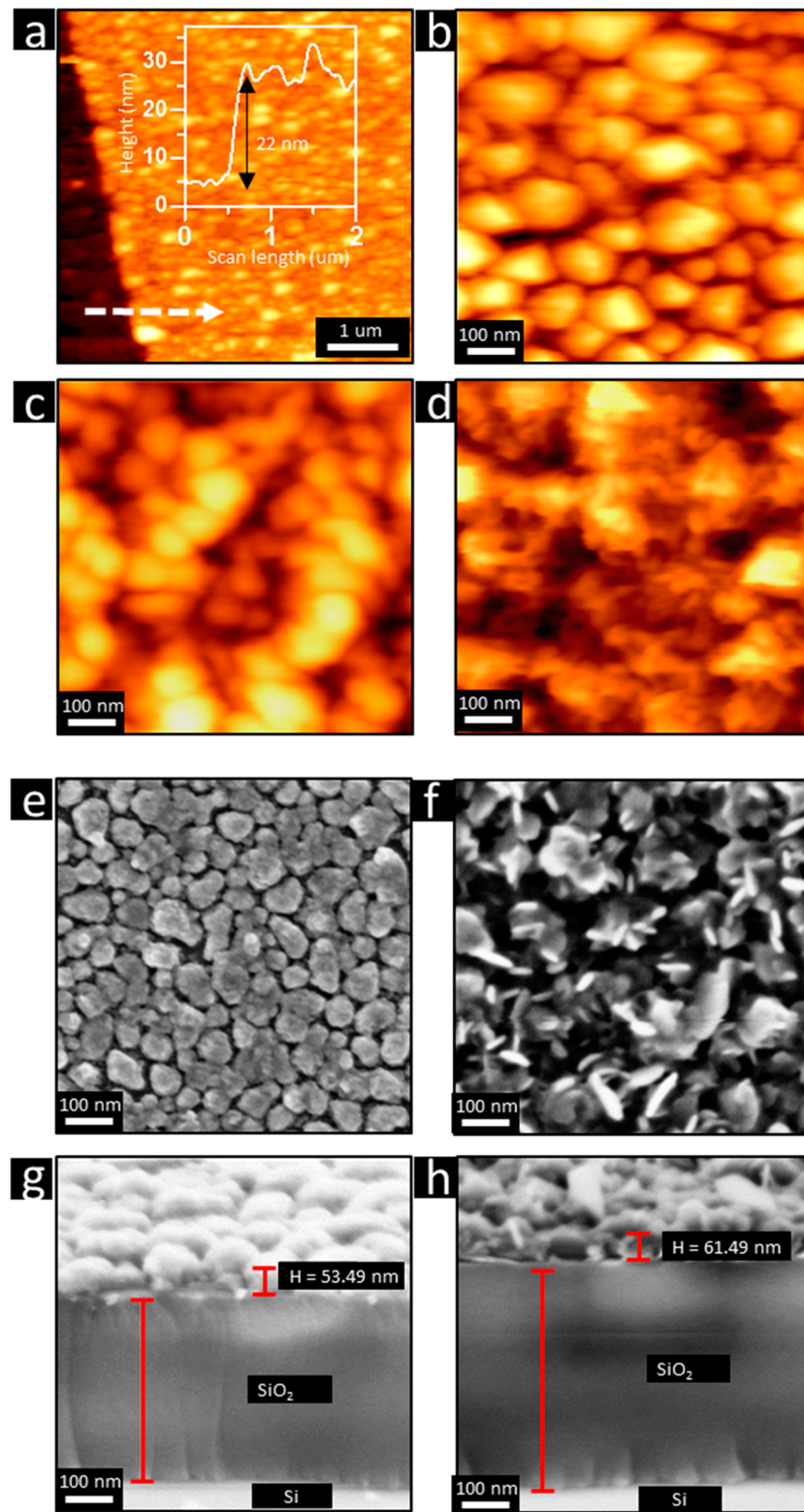


**Figure 4.** (a) AFM image ( $5 \mu\text{m} \times 5 \mu\text{m}$ ) of a pure Sn film. The inset shows the height vs position data corresponding to the line scan (white dashed arrow) across the edge of the film. (b) AFM image of the magnified view of (a) showing the island morphology of the initial Sn film, (c) AFM image, (e) SEM image, (g) SEM cross sectional image of SnS film synthesized at  $150^\circ\text{C}$ , (d) AFM image, (f) SEM image, and (h) SEM cross sectional image of  $\text{SnS}_2$  film synthesized at  $350^\circ\text{C}$ . Scale bars in (a) and (b) are  $1 \mu\text{m}$  and scale bars in (c-h) are  $100 \text{ nm}$ .

(101), (121), (104), and (131). Similarly, for the  $\text{SnS}_2$  film, RHEED reveals (10 $\bar{1}$ 0), (0002), (10 $\bar{1}$ 2), (0003), and (10 $\bar{1}$ 3) peaks in addition to (01 $\bar{1}$ 1) and (11 $\bar{2}$ 0) peaks. In the GIXRD scan of the  $\text{SnS}_2$  film only the (0001) peak of  $\text{SnS}_2$  is observed.

In RHEED the (0001) peak is not observed from the rising intensity near  $0.17 \text{ \AA}^{-1}$ . The theoretical expected (0001) position of  $\text{SnS}_2$  film in RHEED is  $0.1698 \text{ \AA}^{-1}$  as indicated by the dashed line. The reason that the (0001) peak was not

observed was due to the fact that it happens to be lying above the shadowing edge, which means that the outgoing diffraction beam is blocked by the edge of the sample. Aside from that, the results given by RHEED confirm the existence of single phase SnS and single phase SnS<sub>2</sub>, which agrees with the results obtained by GIXRD. Furthermore, the rings exhibited in the RHEED patterns reveal a random orientation in all directions with more peaks as compared with GIXRD scans.

A few RHEED studies of SnS<sub>2</sub> films were reported in the literature, but we are not aware of any for SnS. One example was the molecular beam epitaxy growth of one monolayer to 50 monolayers of SnS<sub>2</sub> on a cleaved mica substrate. The RHEED patterns also contained streaks.<sup>26</sup> The observed streaks imply the top surface of the large ordered layers (50–100 nm) is relatively smooth although the STM/AFM images show island-like features. Another example for SnS<sub>2</sub> is 10 μm thick single crystal 2H-SnS<sub>2</sub> film grown by SnO<sub>2</sub> powders with sulfur and iodine as transporting agents in a silica ampule (845–1035 °C). The RHEED patterns showed elongated streaks perpendicular to the shadowing edge.<sup>45</sup> This implies the film is atomically smooth. Our observed RHEED patterns from SnS and SnS<sub>2</sub> films have concentric rings from randomly oriented grains. These patterns are transmission patterns where electrons transmit through the top of SnS<sub>2</sub> or SnS islands and are not reflection patterns.

**III.C. Morphology of Sn and SnS<sub>x</sub> Films Imaged by Atomic Force Microscopy and Scanning Electron Microscopy.** The surface roughness of a film before it interfaces with another material needs to be minimized. We applied AFM imaging to examine the surface roughness not only in the vertical direction but also the lateral direction as well as local roughness. The vertical roughness (or surface width)  $\omega$ , the lateral correlation length  $\xi$ , and the local short-range roughness parameter  $\alpha$  are analyzed from the height-height correlation analysis.<sup>50</sup> Figure 4a shows an AFM image of a 20 nm Sn/quartz film. A line scan across the edge of the Sn film is indicated by a white dashed arrow. The inset shows the corresponding height versus position data. A ~22 nm step-like rise in height at the edge of the Sn film indicates the thickness of the Sn film is about  $20 \pm 2$  nm. The island like morphology of the Sn film is shown in a magnified image in Figure 4b. Figure 4c and d show AFM images of the single phase SnS film sulfurized at 150 °C and the single phase SnS<sub>2</sub> film sulfurized at 350 °C, respectively. The  $\omega$ ,  $\xi$ , and the  $\alpha$  analyzed from 5 μm × 5 μm AFM images for the Sn, SnS, mixed SnS<sub>x</sub>, and SnS<sub>2</sub> films grown at different temperatures are listed in Table 3. In addition to the vertical roughness obtained from the height-height correlation analysis, the root-mean-square (RMS) roughness values obtained from 5 μm × 5 μm AFM images are also listed for a comparison. The RMS values and  $\omega$  values are in tens of nm. The RMS value from the mixed phase grown at 225 °C is higher than the rest of the films. Since the height-height correlation analysis provides additional roughness information in the lateral direction and short-range roughness characteristics, we learned from Table 3 that the lateral correlation length  $\xi$  increases as the sulfurization temperature increases to 350 °C but decreases at 500 °C. This may be due to the loss of Sn at higher temperatures (the melting temperature of Sn is 232 °C).<sup>2</sup> The lateral correlation length is larger than the vertical average size, as it is not limited by the starting Sn film thickness.

SEM top view images of the single phase SnS film synthesized at 150 °C and the single phase SnS<sub>2</sub> film

**Table 3. Roughness Parameters of Sn and SnS<sub>x</sub> Films on Quartz Substrates Obtained from Height–Height Correlation Analysis and the RMS Values from the AFM Software<sup>a</sup>**

sample	growth temp (°C)	surface width $\omega$ (nm)	lateral correlation length $\xi$ (nm)	local roughness $\alpha$ ( $1 < \alpha < 0$ )	RMS from AFM software (nm)
Sn	20	$8.7 \pm 0.1$	$69.3 \pm 1.2$	0.76	8.9
SnS	150	$12.9 \pm 0.1$	$85.0 \pm 1.7$	0.79	11.9
SnS + SnS <sub>2</sub>	200	$12.5 \pm 0.1$	$109.5 \pm 2.0$	0.80	13.1
SnS + SnS <sub>2</sub>	225	$20.9 \pm 0.3$	$109.3 \pm 2.8$	0.81	21.8
SnS <sub>2</sub>	350	$10.0 \pm 0.1$	$138.4 \pm 4.3$	0.81	10.1
SnS <sub>2</sub>	500	$10.9 \pm 0.1$	$71.7 \pm 1.2$	0.74	11.9

<sup>a</sup>Image areas are 5 μm × 5 μm for both analyses.

synthesized at 350 °C are shown in Figure 4e and f, respectively. The SnS film has isolated islands with isotropic shapes. The SnS<sub>2</sub> film is more anisotropic and appears to have a mixture of sheet-like feature. The SEM cross sectional images of these films are shown in Figure 4g and h, respectively. It also shows the thickness of SnS and SnS<sub>2</sub>, which is about 2–3× thicker than the ~20 nm starting thickness of Sn. Note that the films shown in the SEM images were grown on SiO<sub>2</sub> on Si(100) substrates in order to reduce charging effect as compared with that of the quartz substrate.

We discuss ways to enlarge grain size and to grow single crystal films on either amorphous substrates. In the current manuscript the growth conditions (temperature and synthesis time) for tuning the single phase SnS ultrathin film and single phase SnS<sub>2</sub> ultrathin film have been optimized for a starting Sn film 20 nm thick on an amorphous substrate. Our lateral grain size in the sulfurized SnS<sub>x</sub> films from the AFM images ranges from <100 nm to above 100 nm, depending on the sulfurization temperature. The vertical grain size of the SnS<sub>x</sub> films determined from X-ray fwhm of the Bragg peak is in the ~20 nm range of the starting Sn film thickness. The vertical grain size is limited by the original Sn film thickness, but the lateral grain size is less limited in the direction parallel to the substrate. To increase the vertical and lateral grain sizes in the sulfurized polycrystalline film grown on an amorphous substrate, one can increase the starting thickness of the Sn film and increase the sulfurization time to grow thicker SnS<sub>x</sub> films. We have recently been experimenting with 10, 100, and 200 nm starting Sn film thicknesses. In general, the average grain size increases as the thickness of the film increases. That is, the vertical grain size increases with starting film thickness and the lateral grain size is still between 100 to 200 nm. The limitation might be due to a limited grain growth after the nucleation of grains during the sulfurization. Other researchers have used a different approach, i.e. thermal evaporation of SnS powders on a glass substrate. Several examples have shown that the grain size in the SnS<sub>x</sub> film increases as the substrate temperature increases: (1) The single phase SnS film forms at temperature ≥275 °C and has a grain size ~175 nm.<sup>36</sup> The temperature is about 100 °C higher than needed for our single phase SnS formation from the sulfurization of the Sn film at 150 °C. (2) The grain size of SnS<sub>x</sub> film can be increased with a postannealing at 400 °C for SnS film grown at 285 °C in 4% H<sub>2</sub>S atmosphere.<sup>51</sup> (3) In our past work, we showed that tens of micron-sized ultrathin single crystal SnS<sub>2</sub> flakes can be grown on amorphous substrates by

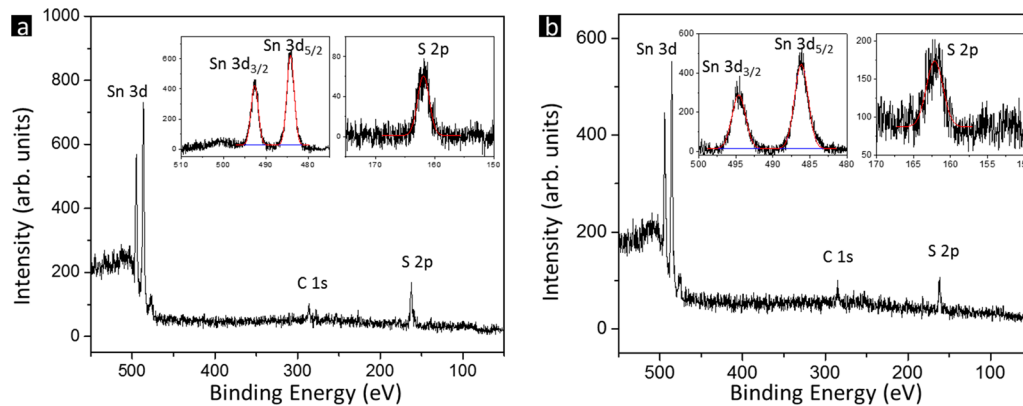


**Figure 5.** X-ray photoelectron spectroscopy spectrum of (a) SnS film synthesized at 150 °C and (b) SnS<sub>2</sub> film synthesized at 350 °C. The red curves in both spectra are Gaussian curve fits that provide the binding energies of Sn and S from the peak positions as well the atomic ratio of Sn to S from the ratio of areas under the fitted curves.

coevaporation of Sn and S at 600 °C.<sup>23</sup> Similar SnS<sub>2</sub> single crystal flakes were grown by chemical vapor deposition;<sup>18</sup> however, these single crystal flakes do not cover the entire substrate.

Materials deposited on amorphous substrates typically do not form single crystalline films rather polycrystalline films are formed. There are ways to overcome the formation of polycrystalline SnS<sub>x</sub> film by using single crystals as substrates. One example is the epitaxial SnS(010) film grown on a single crystal NaCl(100) substrate using vapor transport of SnS powder at 425 °C in a furnace.<sup>16</sup> Other examples are epitaxial SnS films grown on a graphene buffered GaAs(100) substrate held at ~400 °C<sup>52</sup> and on cleaved mica(001) held at ~400 °C<sup>53</sup> by molecular beam epitaxy (MBE). These MBE-grown SnS films have multiple orientational domains due to the symmetry of the crystal substrates. For single crystal SnS<sub>2</sub>, researchers have shown that single crystal SnS<sub>2</sub> tens of microns in size can be grown on mica substrates. However, these flakes do not form a continuous film covering the entire mica substrate.<sup>33</sup> In our group we have demonstrated that biaxial continuous Sn films can be grown on the biaxial CaF<sub>2</sub> buffer layer on an amorphous substrate deposited by oblique angle deposition.<sup>54</sup> One can imagine the possibility of depositing SnS films using SnS powders at an oblique angle deposition on an amorphous substrate to induce a biaxial texture instead of through the sulfurization of predeposited Sn.

**III.D. Chemical Composition of SnS and SnS<sub>2</sub> Films Measured by X-ray Photoelectron Spectroscopy.** XPS is a surface sensitive technique that can reveal near surface chemical composition quantitatively. The shift in binding energy also reveals charge transfer of Sn and S. Figure 5a and b show XPS spectra of single phase SnS and single phase SnS<sub>2</sub> films, respectively. In addition to Sn and S peaks, the C 1s peak is also observed. The binding energy of the C 1s peak (284.8 eV) was used as a reference for binding energy scale calibration. Table 4 lists the measured binding energies of Sn 3d<sub>3/2</sub>, Sn 3d<sub>5/2</sub>, and S 2p peaks for pure Sn and SnS<sub>x</sub> films at various sulfurized temperatures. The composition of these films were determined from  $\frac{\text{Sn}}{\text{S}}$  (atomic ratio) =  $\frac{I_1/S_1}{I_2/S_2}$ , where I<sub>1</sub> and I<sub>2</sub> are relative areas under the respective Sn and S peaks, and S<sub>1</sub> (3.2) and S<sub>2</sub> (0.35) are corresponding sensitivity factors. The last column lists the Sn to S ratio. Experimental Sn/S atomic ratio for single phase SnS is 1.00:1.03. For single phase SnS<sub>2</sub> the ratios are 1.00:2.05 (350 °C) and 1.00:2.06 (500 °C). These

**Table 4. XPS Binding Energies of Sn and S Peaks for the SnS<sub>x</sub> Films**

sulfurization temp (°C)	Sn 3d <sub>3/2</sub>	Sn 3d <sub>5/2</sub>	S 2p	Sn to S ratio
pure Sn (XPS handbook)	493.1	484.6	164.1	
single phase SnS 150	492.5	484.1	161.7	1.00:1.03
mixed phases 200	494.3	485.8	161.9	1.00:1.41
mixed phases 225	493.9	485.4	161.7	1.00:1.66
single phase SnS <sub>2</sub> 350	494.6	486.1	162.1	1.00:2.05
single phase SnS <sub>2</sub> 500	494.5	486.1	162.2	1.00:2.06

values show that the S is slightly rich in single phase films. For mixed phases, the ratios are 1.00:1.41 (200 °C) and 1.00:1.66 (225 °C).

Comparing our measured Sn 3d<sub>5/2</sub> peak at 486.1 eV from single phase SnS<sub>2</sub> film with the measured Sn 3d<sub>5/2</sub> peak at 484.6 eV from pure Sn, the Sn in SnS<sub>2</sub> has a chemical shift of 1.5 eV to a higher value than that of the pure Sn. Comparing the measured S 2p peak at 162.1 eV from single phase SnS<sub>2</sub> film with the measured S 2p peak at 164.1 eV from pure S,<sup>55</sup> the S in SnS<sub>2</sub> has a chemical shift of 1.9 eV to a lower value than that of the pure S. These opposite chemical shifts are consistent with the electron transfers from Sn to S, which form chemical bonds between Sn and S.

**III.E. Raman Spectra of SnS<sub>x</sub> Films.** Raman spectroscopy can reveal local vibrational modes associated with ultrathin crystalline structures. Figure 6 shows the Raman spectra of SnS<sub>x</sub> films sulfurized at 150, 200, 225, 350, and 500 °C. The single phase SnS film synthesized at 150 °C shows two peaks with shoulders; however, four peaks are identified after a peak fit using Gaussian functions. The four vibrational modes are at 157.84, 175.23, 225.19, and 248.57 cm<sup>-1</sup>. As increasing sulfurizing temperature results in a new peak at 314 cm<sup>-1</sup> in addition to these four peaks in the mixed phases. As the sulfurizing temperature increases this 314 cm<sup>-1</sup> peak becomes more intense and the intensity of the four peaks from the SnS film decrease. At temperatures of at least 350 °C, only the 314 cm<sup>-1</sup> peak exists in the single phase SnS<sub>2</sub> film. This trend of single phase SnS, mixed phases of SnS and SnS<sub>2</sub>, and pure phase SnS<sub>2</sub> are consistent with the result of GIXRD. The nature of these vibrational modes are discussed below.

**SnS Film.** In Table 5, the measured Raman peaks from this work, films grown from thermal evaporation of Sn and then sulfurization,<sup>5</sup> thermal evaporation of SnS powders,<sup>6,7</sup> ALD,<sup>14</sup> single crystal,<sup>56</sup> and group theory analysis<sup>57</sup> are listed. Group

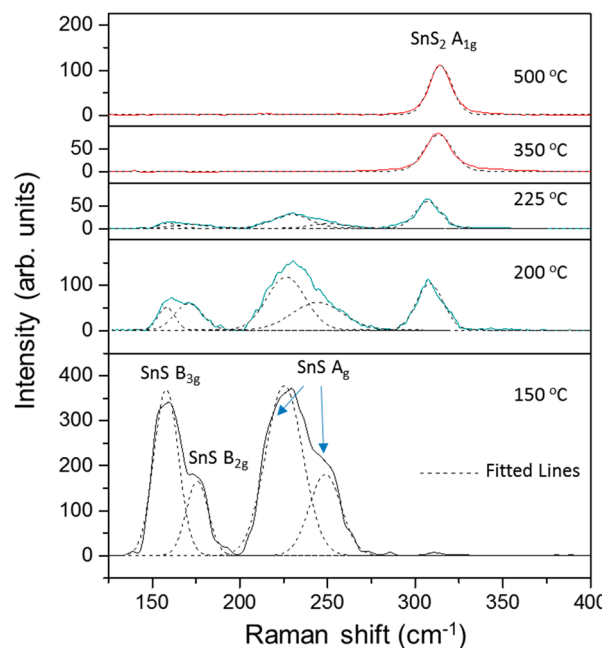


**Figure 6.** Raman spectra of synthesized films measured at room temperature. Synthesized temperatures were 150, 200, 225, 350, and 500 °C. Dashed curves are peak fits. Vibrational modes are labeled and corresponding schematics of vibrations are shown.

theory analysis (the last row in Table 5) reveals that there are nine active longitudinal optic (LO) Raman modes as well as three active transverse optic (TO) Raman modes. For a single crystal, 10 modes were observed, although some are weak.<sup>56</sup> Figure 6 shows our Raman spectra measured from all SnS<sub>x</sub> films. Table 5 lists our observed Raman peaks and results from other works.<sup>2,6,7,14</sup> Our observed Raman peaks are broad (fwhm  $\sim 20$  cm<sup>-1</sup>) and fewer in number than predicted by group theory analysis and collected from a single crystal. We also did not observe peaks at low Raman shifts (below 100 cm<sup>-1</sup>). These may be due to a phonon confinement effect in our ultrathin films.<sup>58</sup> Three of our four Raman peaks at 158, 175, and 225 cm<sup>-1</sup> are within a few cm<sup>-1</sup> of two LO modes (160 and 218 cm<sup>-1</sup>) and one TO mode (178 cm<sup>-1</sup>) from group

theory analysis as well as measurements from a single crystal and films grown by thermal evaporation and ALD. However, our fourth Raman peak located at 248 cm<sup>-1</sup> is substantially lower than that from a single crystal or group theory analysis. There are a couple of reasons that might contribute to the difference. (1) The Raman experiment performed on single crystal SnS by Nikolic et al. in 1977 had a specific scattering geometry. Due to the single crystal with well-defined lattice vectors **a**, **b**, and **c** used in their experiment and group theory analysis, the Raman spectra were collected under X(Y, Z)X scattering geometry, where X, Y, Z, and X̄ represent the incident laser beam direction, polarization vectors of the incident and scattered photons, and the scattered direction of the laser beam, respectively. The laser wavelength they used is 647 nm. A Raman shift at 264 cm<sup>-1</sup> was observed only under the c(a,a)  $\bar{c}$  condition and not in the c(a,b)  $\bar{c}$  or b(a,c)  $\bar{b}$  geometries. This phenomenon is due to the strong in-plane anisotropy in Raman response of single crystal SnS. Our SnS film is not a single crystal but polycrystalline. The major out-of-plane direction is [040] and the in-plane texture is random; therefore, the Raman Ag mode at 264 cm<sup>-1</sup> may not appear if the scattering plane is not exactly at the c(a,a)  $\bar{c}$  condition. In our film, the Raman peak at 248 cm<sup>-1</sup> is a shoulder of the major intense Ag mode centered at 225 cm<sup>-1</sup> after the peak fit of two Gaussians. The fwhms of the peaks located at 225 and 248 cm<sup>-1</sup> are broad with values of  $\sim 25$  and  $\sim 20$  cm<sup>-1</sup>, respectively. A Raman peak at 264 cm<sup>-1</sup> would then be embedded in this broadened shoulder. (2) The Raman shift in the SnS film depends on whether the substrate used is single crystal or amorphous. In our case, the SnS film is ultrathin and the substrate is amorphous SiO<sub>2</sub>. The strain between the ultrathin film and substrate could result in peak broadening and peak shifting.<sup>7</sup>

**SnS<sub>2</sub> Film.** Literature reports on experimental Raman peaks of SnS<sub>2</sub> nanostructures, SnS<sub>2</sub> films, SnS<sub>2</sub> thin single crystal, and SnS<sub>2</sub> single crystal grown by various methods<sup>20,25,18,57,59–62</sup> report peaks at 205, 309, 311, 314–315, and 330 cm<sup>-1</sup>. Examples from sulfurization of thermal evaporation of Sn,<sup>2</sup> thermal evaporation of SnS powders,<sup>6</sup> and a single crystal<sup>57</sup> are listed in the last column of Table 5. Group theory analysis<sup>57</sup> predicted nine normal modes. Among the nine, three are

**Table 5. Comparisons between Selected Experimental Raman Peaks of SnS Film, SnS<sub>2</sub> Film, and SnS<sub>2</sub> Single Crystal, and Group Theory Analysis<sup>a</sup>**

authors	mode	Raman peaks (cm <sup>-1</sup> )				
		SnS		SnS <sub>2</sub>		
this work			158	175	225	248
thermal <sup>2</sup>					218	315
thermal RT <sup>6</sup>			170		238	330
thermal 300 °C <sup>7</sup>	A <sub>g</sub> mode	95		189	219	
	B <sub>2g</sub> mode		161			291
ALD <sup>14</sup>	A <sub>g</sub> mode	68	94	191	219	
	B <sub>2g</sub> mode		162			288
single crystal <sup>56</sup>	A <sub>g</sub> mode	50	111		216	264
	B <sub>2g</sub> mode	47, 78		170	194	
	B <sub>3g</sub> mode	58		160		
single crystal <sup>57</sup>	A <sub>1g</sub> mode					315
	E <sub>g</sub> mode					205
group theory <sup>7,56,63</sup>	LO mode	40, 49, 78, 85	160	192	208, 218	290
	TO mode	95	178			277

<sup>a</sup>The films were grown by various methods (sulfurization of predeposited Sn,<sup>2</sup> thermal evaporation of SnS powders,<sup>6,7</sup> and ALD<sup>14</sup>).

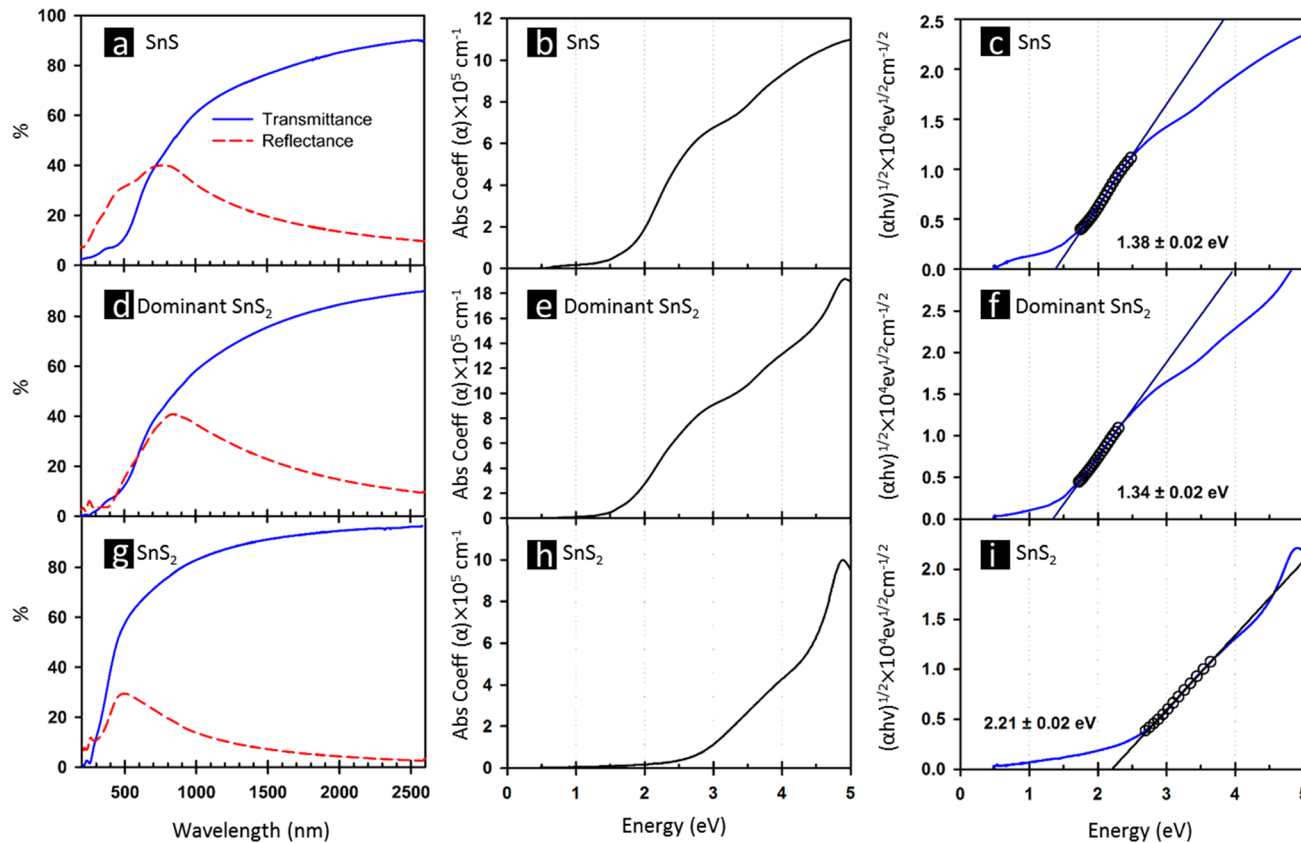


**Figure 7.** UV–vis transmission and reflection spectra (measured at room temperature) of (a) SnS single phase film synthesized at 150 °C, (d) mixed phase of SnS and SnS<sub>2</sub> synthesized at 225 °C, and (g) SnS<sub>2</sub> single phase film synthesized at 350 °C; absorption coefficient vs photon energy of films synthesized at (b) 150, (e) 225, and (h) 350 °C; Tauc plot of film synthesized at (c) 150, (f) 225, and (i) 350 °C.

Raman active modes, A<sub>1g</sub>, with the vibration direction perpendicular to the film surface and a degenerate E<sub>g</sub> mode with the vibration direction parallel to the film surface. The A<sub>1g</sub> mode and the E<sub>g</sub> mode were observed at 315 and 205 cm<sup>-1</sup>, respectively, both at 295 K from a single crystal by the same authors.<sup>57</sup> The short-range force constants from the intra-sandwich Sn–S bond stretching (0.37 N/m), the intersandwich S–S bond stretching (0.18 N/m), and the intra sandwich Sn–S–Sn bond bending (2.72 N/m) were extracted from the fit of a simple model to the measured frequencies. The intersandwich bond stretching is the weakest, consistent with the van der Waal interaction. For our SnS<sub>2</sub> film we observed only the A<sub>1g</sub> mode at 314 cm<sup>-1</sup>, which is lower than 315 cm<sup>-1</sup> from the single crystal<sup>57</sup> and 330 cm<sup>-1</sup> from films grown by thermal evaporation of SnS powders.<sup>6</sup> We did not observe the E<sub>g</sub> mode (205 cm<sup>-1</sup>) observed from a single crystal most likely due to the ultrathin film thickness.<sup>61</sup>

**III.F. Ultraviolet–Visible Spectra of SnS<sub>x</sub> Films.** UV–vis transmission and reflection spectra of all synthesized films were collected in order to determine the optical absorption coefficients vs. wavelength and optical bandgaps. Figure 7a, d, and g show the UV–vis transmission and reflection spectra of three films: SnS single phase film, mixed phase film synthesized at 225 °C, and SnS<sub>2</sub> single phase film synthesized at 350 °C. Figure 7b, e, and h show corresponding absorption coefficients,  $\alpha$  vs photon energy,  $h\nu$ . All absorption plots show coefficient values greater than 10<sup>5</sup> cm<sup>-1</sup> above the optical band gap. The 10<sup>6</sup> cm<sup>-1</sup> absorption coefficient of the mixed phase is even higher than that of the individual single phases in the visible region. This absorption coefficient is higher than the expensive

GaAs in the visible range. Using the Tauc method, plots of  $(\alpha h\nu)^{1/2}$  versus  $h\nu$  are shown in Figure 7c, f, and i. The SnS film, mixed phase film (with a dominant amount of SnS<sub>2</sub>), and SnS<sub>2</sub> film show optical band gaps of  $1.38 \pm 0.02$ ,  $1.34 \pm 0.02$ , and  $2.21 \pm 0.02$  eV, respectively. It is noteworthy that the SnS<sub>2</sub> dominant film has an optical bandgap very close to that of the pure SnS film even though the amount of SnS is smaller than the SnS<sub>2</sub>. The optical absorption coefficient  $\alpha$  of the SnS film is about a factor of 2 stronger than that of the SnS<sub>2</sub> film. The optical bandgap of SnS film (1.38 eV) is also much smaller than SnS<sub>2</sub> film (2.21 eV). Therefore, the Tauc plot of  $(\alpha h\nu)^{1/2}$  is dominated by the existence of SnS in the mixed-phase film of SnS and SnS<sub>2</sub>.

**SnS Film.** The bandgap of SnS has been studied by first-principles DFT. The calculated bandgap depends on the number of layers and the separation between them (strain) as well as surface orientation. The calculated bandgap increases as the number of layers decreases.<sup>64</sup> Specifically, the calculated bandgaps are 1.07, 1.57, and 2.72 eV for the bulk, double-layer and single layer SnS, respectively.<sup>64</sup> The DFT calculated variations of SnS band-edge energies on surface orientation ( $hkl$ ) could be as large as 0.9 eV.<sup>39</sup>

Our measured 1.38 eV optical bandgap of ultrathin SnS film falls between theoretical predicted values of 1.07 and 1.57 eV.<sup>35,64</sup> This implies that our SnS film is thicker than a double layer and closer to tens of layers, consistent with AFM and SEM images and GIXRD vertical crystallite size estimation. The reported experimental values range from 1.08 to 1.70 eV. This wide range of values is understandable from different experimental growth methods that result in different

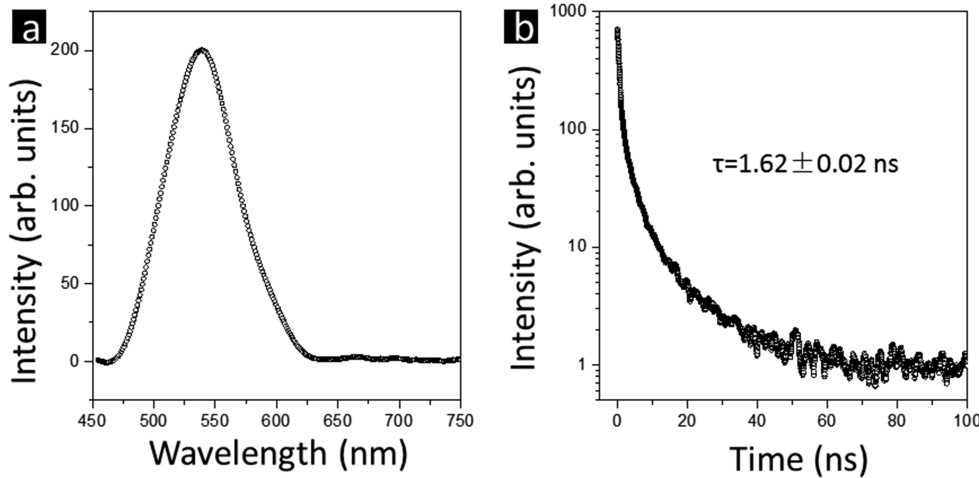


**Figure 8.** (a) PL spectrum and (b) time-resolved PL measured at room temperature. The SnS<sub>2</sub> film was synthesized at 350 °C.

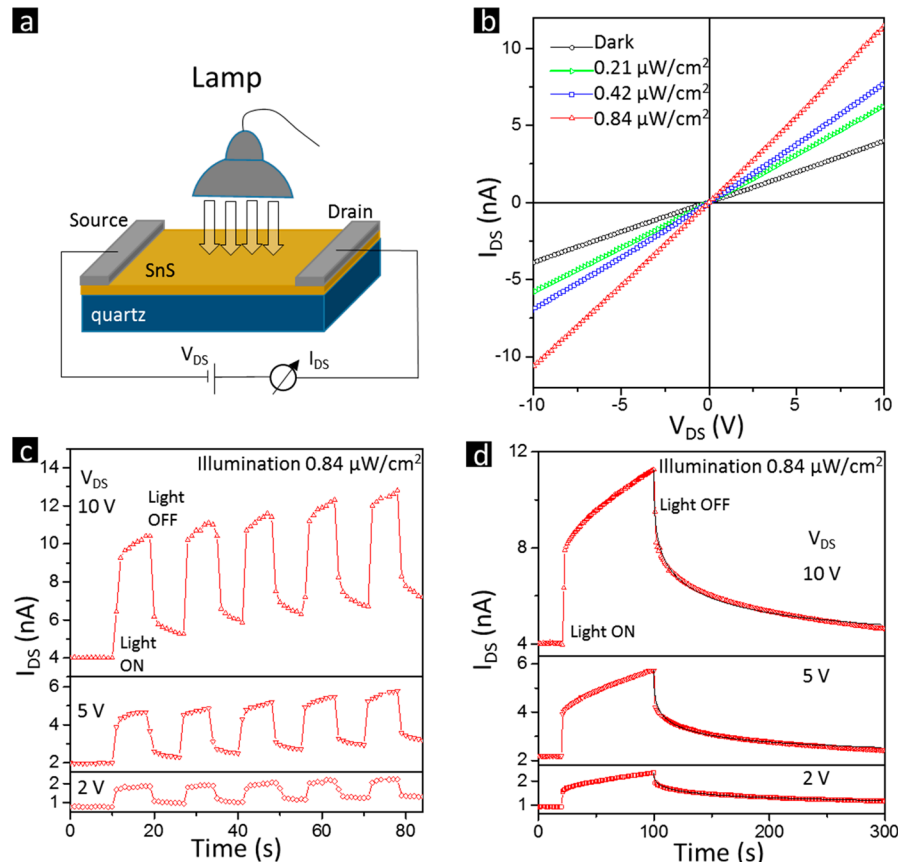


**Figure 9.** (a) Experimental setup for photocurrent vs drain-source voltage ( $I-V_{DS}$ ) measurement using a lamp, (b) current vs voltage of a single phase SnS film under dark and light illumination at 0.21, 0.42, and 0.84  $\mu\text{W}/\text{cm}^2$ , (c) several cycles and (d) one cycle photocurrent responses of single phase SnS film under 0.84  $\mu\text{W}/\text{cm}^2$  illumination at  $V_{DS} = 2$ , 5, and 10 V.

orientations, stoichiometry, and strain. The strain induced change could be up to ~0.5 eV between a few percent positive and negative strains and is dependent on the number of layers.<sup>64</sup>

The coefficient of absorption,  $\alpha$ , of SnS has been calculated by DFT that shows an isotropic gap at 1.16 eV.<sup>65</sup> The value of  $\alpha$  rises rapidly to  $10^5 \text{ cm}^{-1}$  at 2 eV. Our measured  $\alpha$  versus photon energy is qualitatively consistent with the calculation. Our measured  $\alpha$  is  $\sim 2 \times 10^5 \text{ cm}^{-1}$  at 2 eV and  $\sim 7 \times 10^5 \text{ cm}^{-1}$  at 3 eV (see Figure 7b). Typical film thickness for a complete

photon absorption above 1.5 eV in solar cell applications is about 1  $\mu\text{m}$  for an absorption coefficient on the order of  $10^4 \text{ cm}^{-1}$ . In addition, it is beneficial if the difference between measured photon absorption threshold and bandgap is small such as in CdTe, GaAs, and CuInSe. In each of these this difference is about 0.1 eV. If the difference is large, the photon energy is consumed as thermal energy in electrons and holes. For our SnS film, the measured threshold is below 1 eV, below the optical bandgap. This high coefficient of absorption and low threshold implies the film thickness of the absorber layer can be

reduced by 1 order of magnitude from the typical 1  $\mu\text{m}$  thick absorber currently used in solar cells.

***SnS<sub>2</sub>* Film.** Experimental optical bandgaps of SnS<sub>2</sub> reported in the literature ranges from 1.82 to 3.82 eV. The measured optical bandgap depends on the SnS<sub>2</sub> film thickness and growth methods. For example, the value of the band gap decreases from about 2.8 to about 2.1 eV when the thickness increases from a few nm to 1000 nm.<sup>19</sup> Note that the SnS<sub>2</sub> film was grown by a vapor transport method from pure SnO<sub>2</sub> and S powder precursors in a hot-wall quartz tube. The bandgap of bulk SnS<sub>2</sub> has been calculated by DFT to be 2.24 eV.<sup>22</sup> Again our measured optical bandgap of 2.21 eV from ultrathin SnS<sub>2</sub> film falls within the range of experimental numbers but is slightly less than the theoretical predicted value.

**III.G. Photoluminescence Spectra and Time-Resolved PL of SnS<sub>2</sub> Films.** The PL peak position is closely related to the optical bandgap and the time-resolved PL reveals the charge carrier dynamics. The PL spectrum of single phase SnS<sub>2</sub> film synthesized at 350 °C was measured at room temperature with an incident laser of 405 nm wavelength and shown in Figure 8a. One PL peak was observed at  $542.3 \pm 0.2$  nm with a fwhm of  $65.6 \pm 0.5$  nm from the SnS<sub>2</sub> single phase. From  $E_{\text{ph}} (\text{eV}) = \frac{1240}{\lambda(\text{nm})}$ , the peak 542 nm corresponds to a photon energy  $E_{\text{ph}}$  of 2.28 eV, consistent with the optical band gap of SnS<sub>2</sub> film analyzed from UV-vis presented in the previous section. We could not detect a PL signal from ultrathin SnS film due to the sensitivity limit of the photon detector.

We observed only one PL peak at 542 nm (2.28 eV) for the SnS<sub>2</sub> film. Measured PL peaks reported in the literature vary widely from no significant peak,<sup>20</sup> single peak around 625 nm (1.90 eV),<sup>66</sup> two peaks at 526 (2.35 eV) and 819 nm (1.51 eV),<sup>67</sup> two peaks at 620 (2.29 eV) and 700 nm (1.87 eV) for a single crystal,<sup>68</sup> and 551 nm (2.2 eV) from multilayered SnS<sub>2</sub>.<sup>17</sup> These wide variations may be caused by film orientation, mixed phases, crystalline quality, thickness, confinement, defects, and impurities. Theoretical ab initio calculations predicted that SnS<sub>2</sub> is an indirect bandgap semiconductor from bulk to single layer, that is, over the entire thickness range.<sup>17,20</sup> The theoretically calculated direct bandgap of single layer SnS<sub>2</sub> is about 0.3 eV higher than that of indirect bandgap.<sup>69</sup>

Figure 8b shows time-resolved PL measured from the single phase SnS<sub>2</sub> film at 542 nm. A single exponential function was used to fit the time-dependent intensity decay. The fitted decay time for the single phase SnS<sub>2</sub> film is  $1.62 \pm 0.02$  ns. This carrier lifetime in our ultrathin SnS<sub>2</sub> film ( $\sim 50$  nm) is longer than the lifetime of 0.25 ns measured from multilayer SnS<sub>2</sub> film (a few nm thick) reported in the literature.<sup>17</sup> The SnS<sub>2</sub> flakes exhibit increased PL intensity and time-resolved PL carrier lifetime with increasing thickness. This behavior is quite different than is exhibited by MoS<sub>2</sub> flakes. Ultrathin MoS<sub>2</sub> flakes were reported to exhibit an increased PL intensity<sup>70</sup> and a very short carrier lifetime of 5 ps with decreasing thickness.<sup>71</sup> It has been shown that the PL decay lifetime in over 10  $\mu\text{m}$  thick CdTe film is strongly correlated to the open circuit voltage  $V_{\text{oc}}$ . For example, for 2 ns lifetime the corresponding  $V_{\text{oc}}$  is about 0.83 V.<sup>72</sup> Our 1.6 ns associated with ultrathin thin SnS<sub>2</sub> film is potentially a good candidate for solar cell applications.

**III.H. Photocurrent Response vs Voltage of SnS Film.** For potential application of ultrathin SnS film as a photodetector, one needs high current responsivity and fast photoresponse time to illumination. Figure 9a shows the setup for  $I$ – $V$  measurement of single phase SnS film at room

temperature. A household incandescent heat lamp in a round aluminum reflector having a broad range of wavelengths ranging from 500 to 1000 nm was used and the illumination area was about  $0.15 \pm 0.05 \text{ cm}^2$ . The source and drain contact electrodes are made of indium. Figure 9b shows the photocurrent versus drain-source voltage ( $I$ – $V_{\text{DS}}$ ) curves of the single phase SnS film under no (dark) and light illumination. Three light power densities 0.21, 0.42, and 0.84  $\mu\text{W}/\text{cm}^2$  were used. The slopes of  $I$  versus  $V_{\text{DS}}$  under the dark and light illumination are linear indicating good Ohmic contact. This result supports previous work stating that indium creates an excellent Ohmic contact with SnS.<sup>36,73</sup> To form an Ohmic contact between a metal and a semiconductor, the chosen metal's work function,  $\phi_m$  must be close to the work function of SnS or greater than the electron affinity,  $\chi_s$ , of SnS. The work function  $\phi_m$  of indium is 3.83 eV. The work function,  $\phi_s$ , and the electron affinity,  $\chi_s$ , of SnS are 4.2<sup>73</sup> and 3.14 eV,<sup>36</sup> respectively. The slope of  $I$  versus  $V_{\text{DS}}$  increases as the illuminating power increases and bias voltage increases. The inverse of the slope gives the value of resistance. The resistance values under dark conditions and 0.21, 0.42, and 0.84  $\mu\text{W}/\text{cm}^2$  illumination are  $2.57 \times 10^9$ ,  $1.66 \times 10^9$ ,  $1.37 \times 10^9$ , and  $0.91 \times 10^9 \Omega$ , respectively. The resistance of the film under illumination is lower than that of the dark ( $\sim 2.57 \times 10^9 \Omega$ ) condition. This behavior results from that the SnS film absorbing photons that have energy larger than the bandgap. The photons excite electrons from the valence band to the conduction band. The increase of free carrier density in the SnS film can lead to the decreased resistance (increased conductivity).

Figure 9c and d show the on/off photocurrent responses in the single phase SnS film under a fixed 0.84  $\mu\text{W}/\text{cm}^2$  lamp light illumination for several cycles and a single cycle, respectively. The photoresponse current increases as the  $V_{\text{DS}}$  increases from 2 to 5 to 10 V. A critical parameter for a photodetector is the detector's current responsivity  $R$ , defined as the photocurrent generated per unit power of the incident light on the effective area of a photo conductor.  $R$  is expressed as  $R = \Delta I/PS$ , where  $\Delta I$  is the difference between the currents with light on and off shown in Figure 9d.  $P$  is the light power intensity and  $S$  is the effective area of photodetector. The calculated  $R$  for three biases are shown in Table 6. The value of  $R$  increases with

**Table 6. Calculated Current Responsivity  $R$  (under Various  $V_{\text{DS}}$  Voltages), Extracted Decay Time  $\tau_1$ , and the Decay Exponent  $\beta$  from the Fits of Photoresponse Curves in the Decay Region<sup>a</sup>**

$V_{\text{DS}}$ (V)	$R$ (A/W)	decay time fitting parameters		
		$\tau_1$ (sec)	$\beta$	photocurrent on-off ratio
10	0.06	$16.98 \pm 0.34$	$0.403 \pm 0.005$	$1.02 \pm 0.27$
5	0.03	$18.28 \pm 0.39$	$0.345 \pm 0.005$	$1.03 \pm 0.17$
2	0.01	$19.12 \pm 0.41$	$0.366 \pm 0.003$	$0.93 \pm 0.25$

<sup>a</sup>The photocurrent on-off ratio is shown in the last column.

increasing bias voltage  $V_{\text{DS}}$ . The calculated  $R$  is  $\sim 0.06 \text{ A/W}$  (for comparison, the photoresponsivity of ratio of  $R$  over the effective area is  $0.40 \text{ A/W cm}^{-2}$ ) for  $V_{\text{DS}} = 10 \text{ V}$ . For comparison, a photodetector made of a solution synthesis of SnS nanoribbons (2–5  $\mu\text{m}$  long by 150–500 nm wide by  $\sim 10$  nm thick) has a photoresponsivity of  $3 \text{ } \mu\text{A/W cm}^{-2}$ .<sup>74</sup> The value of  $R$  depends on the incident wavelength and bias voltage.

The photocurrent versus time curve shown in Figure 9d has a fast rise ( $\sim 1$  s) when the light is first on and then a slow rise, and a fast drop ( $\sim 1$  s) when the light is off, followed by a slow decay. In order to study recombination processes, the corresponding decay time in the photocurrent is fitted using  $I = I_d + (I_0 - I_d)e^{-(t-t_0/\tau_1)^\beta}$ , ( $0 < \beta < 1$ ). Where  $I_d$  is the current measured under dark conditions (light off),  $I_0$  is the current at the moment  $t_0$  when the light is turned off.  $\tau_1$  is a characteristic constant for the decay of the photocurrent and  $\beta$  is the decay exponent.<sup>75</sup> As shown in Table 6, the decay time is less than 20 s and changes slightly with bias voltage  $V_{DS}$ . Our decay time is comparable to a previous report by Jiang et al. in which photoresponse times of about 40 to 20 s in the slower transient decay regime under the dark condition measured for film thickness ranging from  $\sim 200$ – $1000$  nm.<sup>4</sup> The decay exponent  $\beta$  has a value around 0.4. An exponent less than 1 indicates that the decay time has two distinct periods. When  $t_0 < t < \tau_1$  or  $\frac{t-t_0}{\tau_1} < 1$ , the current drop is fast. For  $\tau_1 < t$  or  $\frac{t-t_0}{\tau_1} > 1$ , the decay is slow. Initially, the photocurrent decays quickly because of the direct recombination of the majority of free electron–hole pairs after the light source is turned off. However, some trapped carriers are untrapped slowly from defect levels in the bandgap with a longer transient time. Similar  $I$ – $V$  curves and photoresponses were measured for the SnS dominant film (resistance  $\sim 7.7 \times 10^8 \Omega$ ) but are not shown here. Our measured transient times are listed in Table 6. Our single phase SnS<sub>2</sub> film did not show any apparent photocurrent under the lamp light but has a weak response under a 405 nm wavelength laser light. The data is not shown here.

The finite transient current decay time after the lamp or laser light has been turned off is a result of charge traps in the SnS film. The photocurrent on–off ratio is defined as  $I_{\text{photon}}/I_{\text{dark}}$ , where  $I_{\text{photon}} = I_{\text{light}} - I_{\text{dark}}$  and  $I_{\text{light}}$  and  $I_{\text{dark}}$  are current when the light is turned on and off. The ratios for the SnS film under  $0.84 \mu\text{W}/\text{cm}^2$  illumination and 2, 5, and 10 V applied voltages are around 1, as shown in Table 6. We are not aware of any literature report on the ratio for the ultrathin SnS film that we can compare to. For films thicker than ours and prepared by other growth methods such as sulfurization of presputtered Sn film in the range of 200–1000 nm, the ratios are  $\sim 0.4$  to 0.6.<sup>29</sup> For 350 nm thick SnS film prepared by pulse electrodeposition on a glass substrate, the ratio is  $\sim 0.2$ .<sup>76</sup> For a 2  $\mu\text{m}$  thick SnS film consisting of 50 nm SnS nanoparticles on an SiO<sub>2</sub>/Si substrate, the ratio is  $\sim 0.24$  measured under a vacuum environment.<sup>30</sup> For the solution synthesis of single crystalline SnS nanoribbons (2–5  $\mu\text{m}$  long by 150–500 nm wide by  $\sim 10$  nm thick), the ratio is  $\sim 0.8$  at 3 V bias voltage.<sup>74</sup> For 1  $\mu\text{m}$  thick SnS film grown by chemical deposition on a glass slide, the ratio is 5 to 10.<sup>77</sup>

## CONCLUSION

A simple method to prepare single phase SnS, single phase SnS<sub>2</sub>, and a mixture of SnS and SnS<sub>2</sub> ultrathin films on quartz substrates is introduced. The properties of films and the SnS/SnS<sub>2</sub> phase ratio in the films can be controlled by simply adjusting the sulfurizing temperature of predeposited ultrathin Sn film. GIXRD and Raman spectra of SnS<sub>x</sub> films indicate that the single phase SnS and single phase SnS<sub>2</sub> films are formed at sulfurizing temperatures of 150 and 350 °C, respectively. The mixed phase SnS and SnS<sub>2</sub> films are obtained at sulfurizing

temperatures of 200 and 225 °C. GIXRD shows that SnS and SnS<sub>2</sub> films have an average vertical crystallite size of about 20 and 10 nm, respectively. The size is limited by the starting Sn film thickness, however, the lateral correlation length is much larger than this. RHEED further reveals that the crystallite orientations are random. UV–vis measurements indicate that the single phase SnS and single phase SnS<sub>2</sub> films have optical bandgaps of  $1.38 \pm 0.02$  eV and  $2.21 \pm 0.02$  eV, respectively. The PL spectrum of SnS<sub>2</sub> has a peak at about 542 nm (2.28 eV). These peaks are consistent with the measured optical bandgap of SnS<sub>2</sub> from UV–vis. Above the optical bandgap, the optical absorption coefficients of SnS<sub>x</sub> films are higher than  $10^5 \text{ cm}^{-1}$ . Time resolved PL shows a decay time of  $1.62 \pm 0.02$  ns for the single phase SnS<sub>2</sub> film. The photoresponse current was observed in the single phase SnS, mixed phase containing SnS, and single phase SnS<sub>2</sub>. The ultrathin continuous single phase SnS and single phase SnS<sub>2</sub> films may contribute to potential applications in optoelectronics and photovoltaics with substantial saving of materials consumption.

## AUTHOR INFORMATION

### Corresponding Author

\*E-mail: yangy20@rpi.edu, yunb.yang@gmail.com. Tel.: +1-5183605852.

### Notes

The authors declare no competing financial interest.

## ACKNOWLEDGMENTS

The work is supported by the New York State Foundation of Science, Technology and Innovation (NYSTAR) through Focus Center-New York, and Rensselaer. P.H.D. acknowledges support from the National Science Foundation CHE-1255100. We thank A. Littlejohn for editing the manuscript and Ping Kuang for useful discussions.

## REFERENCES

- (1) Andrade-Arvizu, J. A.; Courel-Piedrahita, M.; Vigil-Galán, O. SnS-based thin film solar cells: perspectives over the last 25 years. *J. Mater. Sci.: Mater. Electron.* **2015**, *26* (7), 4541–4556.
- (2) Jeng, M. J.; Yang, H. C.; Chang, L. B. Tin sulfide thin films prepared by thermal evaporation and sulfurization. Photovoltaic Specialist Conference (PVSC), 2014 IEEE 40th, Denver, CO, 8–13 June 2014, IEEE, 2014; pp 0379–0381.
- (3) Ramakrishna Reddy, K. T.; Purandhara Reddy, P. Structural studies on SnS films grown by a two-stage process. *Mater. Lett.* **2002**, *56* (1–2), 108–111.
- (4) Jiang, F.; Shen, H.; Wang, W.; Zhang, L. Preparation of SnS film by sulfurization and SnS/a-Si heterojunction solar cells. *J. Electrochem. Soc.* **2012**, *159* (3), H235–H238.
- (5) Klochko, N. P.; Momotenko, O. V.; Tyukhov, I. I.; Volkova, N. D.; Kopach, V. R.; Khrypunov, G. S.; Lyubov, V. M.; Kirichenko, M. V. Structure and properties of SnS thin layers obtained by sulfurization of electrodeposited tin precursors. *Sol. Energy* **2015**, *118*, 117–125.
- (6) Jain, P.; Arun, P. Parameters influencing the optical properties of SnS thin film. *J. Semicond.* **2013**, *34* (9), 093004–1–6.
- (7) Devika, M.; Reddy, N. K.; Prashantha, M.; Ramesh, K.; Reddy, S. V.; Hahn, Y. B.; Gunasekhar, K. R. The physical properties of SnS films grown on lattice-matched and amorphous substrates. *Phys. Status Solidi A* **2010**, *207* (8), 1864–1869.
- (8) Steinmann, V.; Jaramillo, R.; Hartman, K.; Chakraborty, R.; Brandt, R. E.; Poindexter, J. R.; Lee, Y. S.; Sun, L.; Polizzotti, A.; Park, H. H.; Gordon, R. G.; Buonassisi, T. 3.88% Efficient tin sulfide solar cells using congruent thermal evaporation. *Adv. Mater.* **2014**, *26* (44), 7488–7492.

- (9) Park, H. K.; Jo, J.; Hong, H. K.; Song, G. Y.; Heo, J. Structural, optical, and electrical properties of tin sulfide thin films grown with electron-beam evaporation. *Curr. Appl. Phys.* **2015**, *15* (9), 964–969.
- (10) Ran, F.-Y.; Xiao, Z.; Hiramatsu, H.; Ide, K.; Hosono, H.; Kamiya, T. SnS thin films prepared by H<sub>2</sub>S-free process and its p-type thin film transistor. *AIP Adv.* **2016**, *6* (1), 015112.
- (11) Wang, W.; Leung, K. K.; Fong, W. K.; Wang, S. F.; Hui, Y. Y.; Lau, S. P.; Chen, Z.; Shi, L. J.; Cao, C. B.; Surya, C. Molecular beam epitaxy growth of high quality p-doped SnS van der Waals epitaxy on a graphene buffer layer. *J. Appl. Phys.* **2012**, *111* (9), 093520.
- (12) Zhan, X.; Yigang, C. Fabrication of SnS thin films by a novel multilayer-based solid-state reaction method. *Semicond. Sci. Technol.* **2012**, *27* (3), 035007.
- (13) Ham, G.; Shin, S.; Park, J.; Choi, H.; Kim, J.; Lee, Y.-A.; Seo, H.; Jeon, H. Tuning the electronic structure of tin sulfides grown by atomic layer deposition. *ACS Appl. Mater. Interfaces* **2013**, *5* (18), 8889–8896.
- (14) Sinsermsuksakul, P.; Heo, J.; Noh, W.; Hock, A. S.; Gordon, R. G. Atomic layer deposition of tin monosulfide thin films. *Adv. Energy Mater.* **2011**, *1* (6), 1116–1125.
- (15) Ghosh, B.; Das, M.; Banerjee, P.; Das, S. Fabrication and optical properties of SnS thin films by SILAR method. *Appl. Surf. Sci.* **2008**, *254* (20), 6436–6440.
- (16) Wangperawong, A.; Herron, S. M.; Runser, R. R.; Hägglund, C.; Tanskanen, J. T.; Lee, H.-B.-R.; Clemens, B. M.; Bent, S. F. Vapor transport deposition and epitaxy of orthorhombic SnS on glass and NaCl substrates. *Appl. Phys. Lett.* **2013**, *103* (5), 052105.
- (17) Huang, Y.; Sutter, E.; Sadowski, J. T.; Cotlet, M.; Monti, O. L. A.; Racke, D. A.; Neupane, M. R.; Wickramaratne, D.; Lake, R. K.; Parkinson, B. A.; Sutter, P. Tin disulfide—an emerging layered metal dichalcogenide semiconductor: materials properties and device characteristics. *ACS Nano* **2014**, *8* (10), 10743–10755.
- (18) Su, G.; Hadjiev, V. G.; Loya, P. E.; Zhang, J.; Lei, S.; Maharjan, S.; Dong, P.; M. Ajayan, P.; Lou, J.; Peng, H. Chemical vapor deposition of thin crystals of layered semiconductor SnS<sub>2</sub> for fast photodetection application. *Nano Lett.* **2015**, *15* (1), 506–513.
- (19) Ahn, J.-H.; Lee, M.-J.; Heo, H.; Sung, J. H.; Kim, K.; Hwang, H.; Jo, M.-H. Deterministic two-dimensional polymorphism growth of hexagonal n-type sns<sub>2</sub> and orthorhombic p-type SnS crystals. *Nano Lett.* **2015**, *15* (6), 3703–3708.
- (20) Zhang, X.; Meng, F.; Christianson, J. R.; Arroyo-Torres, C.; Lukowski, M. A.; Liang, D.; Schmidt, J. R.; Jin, S. Vertical heterostructures of layered metal chalcogenides by van der waals epitaxy. *Nano Lett.* **2014**, *14* (6), 3047–3054.
- (21) Huang, Y.; Deng, H.-X.; Xu, K.; Wang, Z.-X.; Wang, Q.-S.; Wang, F.-M.; Wang, F.; Zhan, X.-Y.; Li, S.-S.; Luo, J.-W.; He, J. Highly sensitive and fast phototransistor based on large size CVD-grown SnS<sub>2</sub> nanosheets. *Nanoscale* **2015**, *7* (33), 14093–14099.
- (22) Burton, L. A.; Colombara, D.; Abellon, R. D.; Grozema, F. C.; Peter, L. M.; Savenije, T. J.; Dennler, G.; Walsh, A. Synthesis, characterization, and electronic structure of single-crystal SnS, Sn<sub>2</sub>S<sub>3</sub>, and SnS<sub>2</sub>. *Chem. Mater.* **2013**, *25* (24), 4908–4916.
- (23) Yang, Y. B.; Dash, J. K.; Littlejohn, A. J.; Xiang, Y.; Wang, Y.; Shi, J.; Zhang, L. H.; Kisslinger, K.; Lu, T. M.; Wang, G. C. Large single crystal SnS<sub>2</sub> flakes synthesized from coevaporation of Sn and S. *Cryst. Growth Des.* **2016**, *16* (2), 961–973.
- (24) Weidong, S.; Lihua, H.; Haishui, W.; Hongjie, Z.; Jianhui, Y.; Pinghui, W. Hydrothermal growth and gas sensing property of flower-shaped SnS<sub>2</sub> nanostructures. *Nanotechnology* **2006**, *17* (12), 2918.
- (25) Mondal, C.; Ganguly, M.; Pal, J.; Roy, A.; Jana, J.; Pal, T. Morphology controlled synthesis of SnS<sub>2</sub> nanomaterial for promoting photocatalytic reduction of aqueous Cr(VI) under visible light. *Langmuir* **2014**, *30* (14), 4157–4164.
- (26) Schlaf, R.; Louder, D.; Lang, O.; Pettenkofer, C.; Jaegermann, W.; Nebesny, K. W.; Lee, P. A.; Parkinson, B. A.; Armstrong, N. R. Molecular beam epitaxy growth of thin films of SnS<sub>2</sub> and SnSe<sub>2</sub> on cleaved mica and the basal planes of single-crystal layered semiconductors: Reflection high-energy electron diffraction, low-energy electron diffraction, photoemission, and scanning tunneling microscopy/atomic force microscopy characterization. *J. Vac. Sci. Technol., A* **1995**, *13* (3), 1761–1767.
- (27) Sánchez-Juárez, A.; Tiburcio-Silver, A.; Ortiz, A. Fabrication of SnS<sub>2</sub>/SnS heterojunction thin film diodes by plasma-enhanced chemical vapor deposition. *Thin Solid Films* **2005**, *480*–481, 452–456.
- (28) Sinsermsuksakul, P.; Sun, L.; Lee, S. W.; Park, H. H.; Kim, S. B.; Yang, C.; Gordon, R. G. Overcoming efficiency limitations of SnS-based solar cells. *Adv. Energy Mater.* **2014**, *4* (15), 1400496.
- (29) Jiang, F.; Shen, H.; Jiao, J. Formation of photoconductive SnS thin films through reaction of Sn-metal films in sulfur-vapor. *ECS J. Solid State Sci. Technol.* **2013**, *2* (11), P478–P484.
- (30) Lu, F.; Yang, J.; Li, R.; Huo, N.; Li, Y.; Wei, Z.; Li, J. Gas-dependent photoresponse of SnS nanoparticles-based photodetectors. *J. Mater. Chem. C* **2015**, *3* (6), 1397–1402.
- (31) De, D.; Manongdo, J.; See, S.; Zhang, V.; Guloy, A.; Peng, H. High on/off ratio field effect transistors based on exfoliated crystalline SnS<sub>2</sub> nano-membranes. *Nanotechnology* **2013**, *24* (2), 025202–1–6.
- (32) Song, H. S.; Li, S. L.; Gao, L.; Xu, Y.; Ueno, K.; Tang, J.; Cheng, Y. B.; Tsukagoshi, K. High-performance top-gated monolayer SnS<sub>2</sub> field effect transistors and their integrated logic circuits. *Nanoscale* **2013**, *5* (20), 9666–9670.
- (33) Xia, J.; Zhu, D.; Wang, L.; Huang, B.; Huang, X.; Meng, X. M. Large-Scale growth of two-dimensional SnS<sub>2</sub> crystals driven by screw dislocations and application to photodetectors. *Adv. Funct. Mater.* **2015**, *25* (27), 4255–4261.
- (34) Reddy, N. K.; Hahn, Y. B.; Devika, M.; Sumana, H. R.; Gunasekhar, K. R. Temperature-dependent structural and optical properties of SnS films. *J. Appl. Phys.* **2007**, *101* (9), 093522–1–7.
- (35) Vidal, J.; Lany, S.; d'Avezac, M.; Zunger, A.; Zakutayev, A.; Francis, J.; Tate, J. Band-structure, optical properties, and defect physics of the photovoltaic semiconductor SnS. *Appl. Phys. Lett.* **2012**, *100* (1), 032104–1–4.
- (36) Devika, M.; Reddy, K. T. R.; Reddy, N. K.; Ganesan, K. R. R.; Gopal, E. S. R.; Gunasekhar, K. R. Microstructure dependent physical properties of evaporated tin sulfide films. *J. Appl. Phys.* **2006**, *100* (2), 023518–1–7.
- (37) Hartman, K.; Johnson, J. L.; Bertoni, M. I.; Recht, D.; Aziz, M. J.; Scarpulla, M. A.; Buonassisi, T. SnS thin-films by RF sputtering at room temperature. *Thin Solid Films* **2011**, *519* (21), 7421–7424.
- (38) Banai, R. E.; Lee, H.; Motyka, M. A.; Chandrasekharan, R.; Podraza, N. J.; Brownson, J. R. S.; Hom, M. W. Optical properties of sputtered sns thin films for photovoltaic absorbers. *photovoltaics, IEEE Journal of* **2013**, *3* (3), 1084–1089.
- (39) Stevanović, V.; Hartman, K.; Jaramillo, R.; Ramanathan, S.; Buonassisi, T.; Graf, P. Variations of ionization potential and electron affinity as a function of surface orientation: The case of orthorhombic SnS. *Appl. Phys. Lett.* **2014**, *104* (21), 211603–1–4.
- (40) Herring, C. Some theorems on the free energies of crystal surfaces. *Phys. Rev.* **1951**, *82* (1), 87–93.
- (41) Kubaschewski, O.; Evans, E. L. *Materials Thermochemistry*; Pergamon Press: New York, 1958.
- (42) Zhang, Y.; Lu, J.; Shen, S.; Xu, H.; Wang, Q. Ultralarge single crystal SnS rectangular nanosheets. *Chem. Commun.* **2011**, *47* (18), 5226–5228.
- (43) Wang, G.-C.; Lu, T.-M., RHEED transmission mode and RHEED pole figure. *RHEED Transmission Mode and Pole Figures*; Springer, 2014; pp 73–106.
- (44) Ohuchi, F. S.; Parkinson, B. A.; Ueno, K.; Koma, A. van der Waals epitaxial growth and characterization of MoSe<sub>2</sub> thin films on SnS<sub>2</sub>. *J. Appl. Phys.* **1990**, *68* (5), 2168–2175.
- (45) Matsumoto, K.; Kaneko, S. Charaterization of SnS<sub>2</sub> films formed from the vapour phase in a closed tube. *Thin Solid Films* **1984**, *121* (3), 227–232.
- (46) Andrieu, S.; Fréchard, P. What information can be obtained by RHEED applied on polycrystalline films? *Surf. Sci.* **1996**, *360* (1–3), 289–296.
- (47) Litvinov, D.; O'Donnell, T.; Clarke, R. In situ thin-film texture determination. *J. Appl. Phys.* **1999**, *85* (4), 2151–2156.

- (48) Chen, L.; Dash, J.; Su, P.; Lin, C. F.; Bhat, I.; Lu, T. M.; Wang, G. C. Instrument response of reflection high energy electron diffraction pole figure. *Appl. Surf. Sci.* **2014**, *288*, 458–465.
- (49) Drotar, J. T.; Lu, T.-M.; Wang, G.-C. Real-time observation of initial stages of copper film growth on silicon oxide using reflection high-energy electron diffraction. *J. Appl. Phys.* **2004**, *96* (12), 7071–7079.
- (50) Zhao, Y.-P.; Wang, G.-C.; Lu, T.-M. *Characterization of Amorphous and Crystalline Rough Surface: Principles and Applications*; Academic Press, 2001; Vol. 37.
- (51) Chakraborty, R.; Steinmann, V.; Mangan, N. M.; Brandt, R. E.; Poindexter, J. R.; Jaramillo, R.; Mailoa, J. P.; Hartman, K.; Polizzotti, A.; Yang, C.; et al. Non-monotonic effect of growth temperature on carrier collection in SnS solar cells. *Appl. Phys. Lett.* **2015**, *106* (20), 203901.
- (52) Leung, K. K.; Wang, W.; Shu, H.; Hui, Y. Y.; Wang, S.; Fong, P. W. K.; Ding, F.; Lau, S. P.; Lam, C.-h.; Surya, C. Theoretical and experimental investigations on the growth of SnS van der Waals epitaxies on graphene buffer layer. *Cryst. Growth Des.* **2013**, *13* (11), 4755–4759.
- (53) Wang, S. F.; Fong, W. K.; Wang, W.; Surya, C. Growth of highly textured SnS on mica using an SnSe buffer layer. *Thin Solid Films* **2014**, *564*, 206–212.
- (54) Dash, J. K.; Chen, L.; Lu, T. M.; Wang, G. C.; Zhang, L. H.; Kisslinger, K. Metal-enhanced Ge<sub>1-x</sub>Sn<sub>x</sub> alloy film growth on glass substrates using a biaxial CaF<sub>2</sub> buffer layer. *CrystEngComm* **2014**, *16* (37), 8794–8804.
- (55) Wagner, C. D.; Riggs, W. M.; Davis, L. E.; Moulder, J. F.; Muilenberg, G. E. *Handbook of X-ray Photoelectron Spectroscopy*; Perkin-Elmer Corporation, 1978.
- (56) Nikolic, P. M.; Mihajlovic, P.; Lavrencic, B. Splitting and coupling of lattice modes in the layer compound SnS. *J. Phys. C: Solid State Phys.* **1977**, *10*, L289.
- (57) Smith, A. J.; Meek, P. E.; Liang, W. Y. Raman scattering studies of SnS<sub>2</sub> and SnSe<sub>2</sub>. *J. Phys. C: Solid State Phys.* **1977**, *10* (8), 1321–1323.
- (58) Sohila, S.; Rajalakshmi, M.; Ghosh, C.; Arora, A. K.; Muthamizhchelvan, C. Optical and raman scattering studies on SnS nanoparticles. *J. Alloys Compd.* **2011**, *509* (19), 5843–5847.
- (59) Wang, C.; Tang, K.; Yang, Q.; Qian, Y. Raman scattering, far infrared spectrum and photoluminescence of SnS<sub>2</sub> nanocrystallites. *Chem. Phys. Lett.* **2002**, *357* (5–6), 371–375.
- (60) Rout, C. S.; Joshi, P. D.; Kashid, R. V.; Joag, D. S.; More, M. A.; Simbeck, A. J.; Washington, M.; Nayak, S. K.; Late, D. J. Enhanced field emission properties of doped graphene nanosheets with layered SnS<sub>2</sub>. *Appl. Phys. Lett.* **2014**, *105* (4), 043109–1–5.
- (61) Zhou, X.; Zhang, Q.; Gan, L.; Li, H.; Zhai, T., Large-size growth of ultrathin SnS<sub>2</sub> nanosheets and high performance for photo-transistors. *Adv. Funct. Mater.* **2016**, DOI: [10.1002/adfm.201600318](https://doi.org/10.1002/adfm.201600318), in press.
- (62) Burton, L. A.; Whittles, T. J.; Hesp, D.; Linhart, W. M.; Skelton, J. M.; Hou, B.; Webster, R. F.; O'Dowd, G.; Reece, C.; Cherns, D.; et al. Electronic and optical properties of single crystal SnS<sub>2</sub>: an earth-abundant disulfide photocatalyst. *J. Mater. Chem. A* **2016**, *4* (4), 1312–1318.
- (63) Chandrasekhar, H.; Humphreys, R.; Zwick, U.; Cardona, M. Infrared and raman spectra of the IV-VI compounds SnS and SnSe. *Phys. Rev. B* **1977**, *15* (4), 2177–2183.
- (64) Tritsaris, G. A.; Malone, B. D.; Kaxiras, E. Optoelectronic properties of single-layer, double-layer, and bulk tin sulfide: A theoretical study. *J. Appl. Phys.* **2013**, *113* (23), 233507–1–8.
- (65) Makinistian, L.; Albanesi, E. A. On the band gap location and core spectra of orthorhombic IV–VI compounds SnS and SnSe. *Phys. Status Solidi B* **2009**, *246* (1), 183–191.
- (66) Joshi, P. D.; Joag, D. S.; Rout, C. S.; Late, D. J. Photosensitive field emission study of SnS<sub>2</sub> nanosheets. *J. Vac. Sci. Technol. B* **2015**, *33* (3), 03C106–1–4.
- (67) Manoharan, C.; Kiruthigaa, G.; Dhanapandian, S.; Kumar, K. S.; Jothibas, M., Preparation and characterization of nanostructured SnS<sub>2</sub> by solid state reaction method. ICANMEET-2013; *Proceedings of the International Conference on Advanced Nanomaterials and Emerging Engineering Technologies*; IEEE, 2013; pp 30–33.
- (68) Kuzuba, T.; Era, K.; Ishizawa, Y. Photoluminescence of SnS<sub>2</sub> single crystals. *Phys. Lett. A* **1974**, *46* (6), 413–414.
- (69) Zhuang, H. L.; Hennig, R. G. Theoretical perspective of photocatalytic properties of single-layer SnS<sub>2</sub>. *Phys. Rev. B: Condens. Matter Mater. Phys.* **2013**, *88* (11), 115314–1–5.
- (70) Splendiani, A.; Sun, L.; Zhang, Y.; Li, T.; Kim, J.; Chim, C.-Y.; Galli, G.; Wang, F. Emerging photoluminescence in monolayer MoS<sub>2</sub>. *Nano Lett.* **2010**, *10* (4), 1271–1275.
- (71) Korn, T.; Heydrich, S.; Hirmer, M.; Schmutzler, J.; Schüller, C. Low-temperature photocarrier dynamics in monolayer MoS<sub>2</sub>. *Appl. Phys. Lett.* **2011**, *99* (10), 102109.
- (72) Metzger, W.; Albin, D.; Levi, D.; Sheldon, P.; Li, X.; Keyes, B.; Ahrenkiel, R. Time-resolved photoluminescence studies of CdTe solar cells. *J. Appl. Phys.* **2003**, *94* (5), 3549–3555.
- (73) Devika, M.; Reddy, N. K.; Patolsky, F.; Gunasekhar, K. Ohmic contacts to SnS films: Selection and estimation of thermal stability. *J. Appl. Phys.* **2008**, *104* (12), 124503–1–6.
- (74) Deng, Z.; Cao, D.; He, J.; Lin, S.; Lindsay, S. M.; Liu, Y. Solution synthesis of ultrathin single-crystalline SnS nanoribbons for photodetectors via phase transition and surface processing. *ACS Nano* **2012**, *6* (7), 6197–6207.
- (75) Dang, X.; Wang, C.; Yu, E.; Boutros, K.; Redwing, J. Persistent photoconductivity and defect levels in n-type AlGaN/GaN heterostructures. *Appl. Phys. Lett.* **1998**, *72* (21), 2745–2747.
- (76) Mathews, N.; Anaya, H. B.; Cortes-Jacome, M.; Angeles-Chavez, C.; Toledo-Antonio, J. Tin sulfide thin films by pulse electro-deposition: structural, morphological, and optical properties. *J. Electrochem. Soc.* **2010**, *157* (3), H337–H341.
- (77) Nair, M. T. S.; Nair, P. K. Simplified chemical deposition technique for good quality SnS thin films. *Semicond. Sci. Technol.* **1991**, *6* (2), 132–134.